2013

Phase field approach for melting of aluminum nanoparticles

Kamran Samani
Iowa State University

Phase field approach for melting of aluminum nanoparticles

by

Kamran Samani

A thesis submitted to the graduate faculty

in partial fulfillment of the requirements for the degree of

DOCTOR OF PHILOSOPHY

Major: Mechanical Engineering

Program of Study Committee:

Valery I. Levitas, Major Professor

Ashraf Bastawros

Abhijit Chandra

Baskar Ganapathysubramanian

Wei Hong

Iowa State University

Ames, Iowa

2013

DEDICATION

I would like to dedicate this thesis to my mother

and the memory of my father

for their love, patience and sacrifice.

TABLE OF CONTENTS

LIST OF FIGURES

ACKNOWLEDGEMENTS

I would like to take this opportunity to express my thanks to those who helped me with various aspects of conducting the research and the writing of this thesis. First and foremost, Dr. Valery Levitas for his guidance and support throughout this research. I would also like to thank my committee members: Dr. Ashraf Bastawros, Dr. Abhijit Chandra, Dr. Baskar Ganapathysubramanian and Dr. Wei Hong.

CHAPTER 1. GENERAL INTRODUCTION

Introduction

Aluminum nanoparticles are of interest due to the variety of their applications, including additives for plastics and powder metallurgy. They can also enhance the burning rate of propellants. Metallic particles in traditional thermites are in the micron size range $1 - 100\mu m$. When the particle diameter reduces to the nanometer range $20 - 120nm$, their reactivity increases by several orders of magnitude. Thus flame rates of $0.9 - 1km/s$ can be reached, while for micron size thermites they are on the order of centimeters or meters per second. Ignition delay time also decreases by up to three orders of magnitude.

The two main continuum methods to study melting-related phenomena (like surface melting, size dependence of melting temperature, melting of a few nm-size particles, and overheating at a very fast heating rate) are the sharp interface method and the phase field approach. The sharp interface approach fails when nanoparticles and solid-liquid interface radii are comparable with interface width and also when nanoparticles are overheated fast. In the phase field model, the interface between phases has a finite thickness in which physical quantities, such as elastic moduli and entropy, vary between their values in the adjacent bulk phases. The order parameter, η describe the material instabilities, such as the instabilities of a crystal lattice in solidsolid phase transformations, melting, fracture and so on. Phase field method provides smooth description of the phase interface, rather than discontinuous one, as shown below.

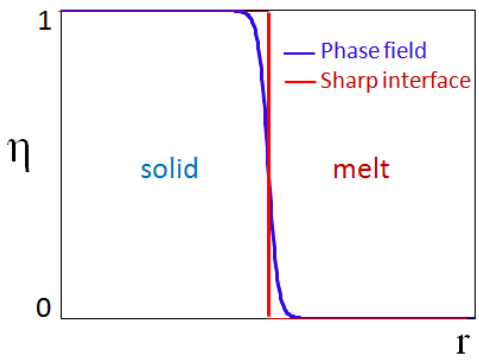

Figure 1.1 Solid-melt interface, phase field approach vs. sharp interface model.

We developed an advanced phase field model coupled to mechanics to study melting in the region of metastability and complete instability of solid and melt.

Litereature Review

Experimental studies

It was first shown experimentally in 1954 that the melting temperature of ultrafine particles is below that of bulk material. Takagi[62] used electron diffraction method to study structure change of thin films of Pb, Sn and Bi. The mean thickness of the films ranged from 1nm to 100nm. She took the radius of the particle to be equal to the mean thickness of the film. The study confirmed that the melting temperature decreases proportional to the reciprocal of the particle radius.

Electron diffraction method was used by Coombes[15] to investigate melting temperature of Pb and In. He also obtained the thickness of liquid layer for Pb at equilibrium melting to be 3nm. Gladkich et.al.[23] used the same technique for Cu, Al and Ge. Further references to earlier works using electron diffraction and electron microscopy method for different nanoparticles are mentioned in the paper by Jesser et al.[27].

Frenken and van der Veen[22] used ion shadowing and blocking measurements to show that the solid-liquid transition at the surface of a three dimensional crystal, Pb(110),

starts at 40K below the melting temperature of the bulk lead. Devaud and Willens [17] used transmission electron microscopy and observed a broadened melting transition of 2nm uniformly flat Pb film, sandwiched between two Ge films. The breadth of the transition was found to be 40K. The transition was found to be continuous and reversible.

Ajayan and Marks[1] presented experimental evidence that small particles on substrate sit in deep potential energy wells and when floated out, can quasimelt between various local minima free energy surfaces. The energy needed to nucleate the quasimolten state was found to be orders of magnitude larger than that needed to sustain the state. The particles remain in unstable state for a long time before they find another well on the substrate.

Castro et al.[9] considered gold and silver clusters with diameter in the nanometer range, deposited on tungsten. Although they did not include the effect of substrate on melting, they obtained good agreement with experimental results for Au and Ag clusters with diameter greater than 2nm. Lai et al.[34] used scanning calorimetric technique for the melting of nanoparticles of Sn with radii ranging from 5nm to 50nm and showed that the latent heat is also particle size dependent.

Chattopadhyay and Goswami[24, 11] studied melting of nanodispersed Pb and Bi particles in different matrices and showed importance of the crystallographic shape in the melting transition. The melting of the embedded particles was studied by differential scanning calorimetry. Sheng et al.[60] used differential scanning calorimetry to show that the enhancement or depression of the melting temperature of embedded In nanoparticles (5-45 nm) depends on the epitaxy between the nanoparticles (In) and the embedding matrix (Al).

Peters et al.[49, 50] used x-ray powder diffraction in ultrahigh vacuum for Pb crystallites of 50nm diameter and compared results with those from Lereah et al.[36] who used dark-field transmission electron microscopy on a 100 nm Pb particle constrained in a solid silica overlayer. The liquid skin thickness change was much larger from Lereah et al.

than what they detected in measurements. They mentioned that the large difference in results can be because of silica matrix, and that the hydrostatic stresses exerted on the Pb particles due to thermal expansion mismatch can shift the melting temperature. It was also shown that crystallite reorientation makes the diffraction intensity an unreliable indicator of melting. Instead of the diffraction intensity, the diffraction peak shape reveals the size-dependent melting via changes in the crystallite size distribution.

Bachels et al.[3] studied melting of isolated tin nanoparticles in a molecular beam experiment by calorimetrically measuring the clusters' formation energies as a function of their internal temperature. They used the analytical method of Kofman[32] and verified the nonlinear dependence of the melting temperature on the inverse cluster radius and the critical radius for which the cluster will directly transform from the totally solid to the liquid state at the melting temperature.

Lai et al.[35] used calorimetry to obtain melting point depression of Al nanoclusters which form discontinuous Al films over a range of thicknesses from 6 to 50 $\mathring{A}$ on Si_3N_4 surface. The melting point decreased by as much as 140 °C for 2 nm clusters. Dippel et al.[19] measured the melting temperature of nanoscale indium islands on a WSe_2 substrate using perturbed angular correlations combined with scanning tunneling microscopy. Diameter of indium islands ranged from 5nm to 100nm. The relatively small melting point depressions observed in this work were not clearly explained by the classical thermodynamic considerations of melting and premelting.

Dick et al.[18] reported the size dependence of the melting temperature of silica-encapsulated gold nanoparticles. The melting point was determined using differential thermal analysis coupled to thermal gravimetric analysis techniques. The gold particles with sizes ranging from 1.5 to 20 nm were coated with porous silica shells to isolate the particles from one another. The silica shell acts as a nanocrucible for the melting gold with little effect on the melting temperature.

Jesser et al.[27] studied the melting behavior of isolated nanoparticles of Pb-Bi alloys

with radii ranging from 5nm to 40nm, by hot stage transmission electron microscopy. From the experimental data, phase diagrams of individual, isolated nanoparticles were constructed as a function of the size of the nanoparticle. The liquid and solid phases follow melting paths that form liquidus and solidus bands on the temperature-composition phase diagram. The range of two-phase coexistence shrinks as the solute concentration decreases, and the liquidus and solidus bands finally coalesce into a single line at low solute concentrations in apparent violation of the Gibbs phase rule.

Mei et al.[43] studied melting and superheating behavior of Al nanoparticles encapsulated in Al_2O_3 shells by X-ray diffraction. Experimental results revealed that the encapsulated Al nanoparticles with different particle sizes can be superheated to 7-15K beyond the bulk equilibrium melting point of Al, accompanied with a suppressed thermal expansion behavior. A value for the pressure build-up on the Al core due to the constraint of the rigid Al_2O_3 shell of up to 0.25GPa was derived from the temperature dependence of lattice spacing for the superheated samples.

Trunov et al.[64] investigated the melting and oxidation behavior of nanosized aluminum powders by differential scanning calorimetry. The oxidation was observed to begin at the temperatures substantially lower than the onset for the melting and no correlation between melting and oxidation was observed, similar to the results for the micron-sized Al powders. Ruan et al.[55] have experimentally observed the reversible surface premelting of Au nanoparticles (2-20 nm) under femtosecond laser irradiation using ultrafast electron nanocrystallography.

Sun and Simon[61] studied the melting behavior of aluminum nanoparticles having an oxide passivation layer using differential scanning calorimetry. The melting point depression, both corrected and uncorrected for the effects of the oxide shell, was linear with the reciprocal of particle radius, as predicted by Gibbs-Thomson equation. The size-dependent heat of fusion was significantly smaller than that predicted by the effects of the surface tension, indicating that the solid nanoparticle was at a higher energy

than expected, presumably due to the presence of defects or irregularities in the crystal structure at or emanating from the surface.

Levitas et al.[40] studied the dependence of aluminum melting temperature on particle size for particles encapsulated in an oxide shell using differential scanning calorimeter and thermogravitmetric analyzer. Mechanical damage in the oxide shell was shown to reduce the melting temperature due to a decrease in generated pressure within the Al core. Zou et al.[72] studied synthesized tin nanoparticles by differential scanning calorimetry. The results showed that the cube root of the latent heat of fusion of Sn nanoparticles was linearly dependent on the reciprocal of the average particle diameter.

In conclusion, the experimental studies show dependence of melting temperature of nanoparticles on particle size. Also, they show that surface melting occurs only for particles with radius larger than a critical value which depends on the material.

Theoretical studies

The size dependence of melting temperature of a very small crystal was discussed by Pawlow[48] using a homogeneous melting model without a liquid skin. He obtained an equation for the melting point (triple point) in which spherical solid and liquid were in equilibrium with vapor, The relative surface energies of the liquid and crystal phase are such that a decrease of the melting temperature would be expected.

Rie[53] mentioned that because the solid sphere is covered by a layer of melt, Pawlow's assumption of solid-liquid-vapor equilibrium is not correct. He derived an equation for the melting temperature that showed an inverse relation between the decrease of the melting temperature and the particle size. Reiss and Wilson[54] used the standard theory of equilibrium thermodynamics to obtain an equation for the equilibrium temperature between molten layer and solid core for a indefinitely thin shell. Blackman and Curzon[5] extended this equation to describe their experimental results for Sn where transmission electron diffraction was used to detect melting. Wronski[68] pointed out that in the case

of a real liquid it is necessary to assume a finite size for a critical nucleus of liquid. The magnitude of this critical thickness was determined by fitting the theory to the experimental results and the value obtained from experiment was about 3nm for tin. He obtained an equation in which the melting temperature decreased more rapidly than the increase in 1/R, as opposed to the results of Blackman and Curzon who obtained a linear relation between melting temperature and l/R.

Buffat and Borel[8] used scanning electron diffraction technique for gold particles with diameters down to 2nm and compared their results with two models. The first model describes the equilibrium condition for system formed by a solid particle, a liquid having the same mass and their saturation vapor phase. The second model assumed the preexistence of a liquid layer surrounding the solid particle which describes the equilibrium of such system in the presence of a vapor phase. The experimental results were found to agree closely with predictions of the first model provided that physical constants for gold were the known values appropriate to the massive metal. The results were in agreement with the second model if the thickness of the liquid layer was given the value of $6.2\mathring{A}$.

Couchman and Jesser[16] considered the formation, nucleation and growth of liquid layer in their model and compared the predictions of this theory with experimental results for Sn, In and Au. They concluded that the critical liquid thickness is not constant for each metal but decreases monotonically with decreasing the particle size. Vanfleet and Mochel[65] reexamined a thermodynamic model for small particles and added a surface melting interaction. This model predicts an energy barrier between the liquid and solid states. For particles below a certain size this barrier is easily surmounted in either direction. Above this critical size the barrier results in a difference between the melting and freezing points. They proposed to use the same nucleation and growth requirement for freezing as Couchman[16] required for melting.

Johari[30] mentioned previous analytical equations for melting temperature suppression and analytically calculated change in physical parameters like entropy and enthalpy of

Au particle with a radius of 1μm. Kofman et al.[33] introduced a short range interaction between both solid/liquid and liquid/vapor interfaces. This interaction was described by a characteristic length, to obtain a minimum in the free energy of the three-phase system. They[32] used their earlier model to compare with experimental results for Pb and concluded that when the inner solid core reaches a critical radius, melting occurs discontinuously and irreversibly.

Nanda et al.[45] established an empirical relations between the cohesive energy, surface tension and melting temperature of different bulk solids. On the basis of an analogy with the liquid-drop model and these empirical relations, and compared with other theoretical models and available experimental data, an expression for the size-dependent melting was derived. Jiang et al.[28] described a model for size-dependent melting of organic nanocrystals, and checked it with experimental results for benzene, heptane and naphtalene nanocrystals. They also extended the model[29] for polyethylene. As diameter decreased below 3nm, the model could not interpret experimental data because the interaction between the lamellae and the surrounding was neglected.

Qi[52] obtained melting temperature of nanoparticles using size-dependent cohesive energy, as it is known that both the cohesive energy and the melting temperature are parameters to describe the bond strength of materials, and it is reported that the cohesive energy has linear relation to the melting temperature for a material. Wautelet[67] studied the variation of the melting temperature of polyhedral elemental nanosolids theoretically. He concluded that in most cases, the size variation of the melting temperature of a sphere is less than for the other shapes, however, there is no general rule regarding the order of the shape parameters of the polyhedra. Safaei et al.[56] considered cohesive energy to obtain melting temperature, taking into account the effect of lattice and surface packing factors, and the coordination number of the lattice and surface crystalline planes. A general equation was proposed, having nonlinear form as a function of the reciprocal of nanosolid size.

Eroshenko[21] obtained results that show clusters consisting of 17 gallium atoms do not undergo melting even at a temperature of 800K, but clusters consisting of 40 atoms are melted at 550K, whereas the melting temperature of macroscopic gallium samples is only 303K. To explain this, Balmakov[4] mentioned a theoretical explanation for the possibility of melting a nanoparticle at a higher temperature as compared to the melting temperature of a macroscopic sample of the same chemical composition.

Wu et al.[69, 70] studied the two-phase Stefan problem for the melting of a spherical nanoparticle by including the effects of interfacial tension and by solving the resulting model with a numerical method. The predictions of the model indicate that it is possible for the temperature in the core particle to be higher than the temperature at the solid-melt interface, and even higher than the temperature in the melted liquid phase near the interface. Also increasing the interfacial tension increases the speed of the solid-melt interface, and thus speeds up the entire melting process.

Due to their different hypotheses, theoretical models, agree well or less well with the experimental results. A linear relationship between melting temperature and 1/R is most commonly proposed. Still not all models support such linear relation.

Molecular dynamics simulations

Ercolessi et al.[20] used molecular dynamics simulations to obtain melting temperature of small gold particles of 100-900 atoms. The results they obtained were consistent with experimental results of Buffat and Borel[8]. They also predicted size dependent depression of latent heat. They showed that in this size range, a sharp melting transition can be identified in contrast to the behavior of clusters with 10-20 atoms. Chushak and Bartell[14] used molecular dynamics simulations to study structures and properties of gold nanoclusters during heating and cooling. The increased depression of melting point as particle size decreases was interpreted in terms of Pawlow's triple point theory, the liquid shell model, and extensions of the two.

Zhao et al.[71] studied the melting properties of isolated silver nanoparticles using molecular dynamics simulations. Three distinctive melting mechanisms were identified. The melting of Ag with 258-3871 atoms were explained well by the surface premelting models while the melting of Ag with 13-178 atoms could be described as a transition from a low-energy solidlike structure at low temperatures to a higher-energy liquidlike structure at high temperatures. Acting as a connecting link between such two distinctive melting mechanisms, a new intermediate melting mechanism, in which the melting temperature depressed very slowly while the latent heat of fusion had a great enhancement with N decreasing, was identified in Ag with 120-240 atoms.

Alavi and Thompson[2] used molecular dynamics simulations to determine the melting point of aluminum nanoparticles. Nanoparticles with less than 800 atoms ($\approx 25\mathring{A}$) showed bistability between the solid and liquid phases over temperature ranges below the point of complete melting. This bistability is characteristic of dynamic coexistence melting. The temperature range of bistability becomes narrower and shifts to higher temperatures as the size of the nanoparticle increases. Nanoparticles of Al larger than $25\mathring{A}$ exhibited surface premelting behavior. Puri and Yang[51] used molecular-dynamics simulations to predict the melting of nanosized aluminum particles. Sharp variations in structural and thermodynamic properties were found across the melting point for a bulk material. In contrast, only smooth changes were observed for nanoparticles, due to the presence of surface premelting.

Wang et al.[66] used molecular dynamics simulations for reversible nonhomogeneous surface premelting of Au nanoparticles with radii of 1.22 to 4.49 nm. They concluded that the melting initiates on the surface of a nanoparticle and liquid-like atoms start to appear on edges of surface facets. For larger Au nanoparticles like N $>$ 7164 (R $>$ 3.07nm), the surface was completely premelted whereas for smaller nanoparticles like N = 456 (R = 1.22nm) , it was only partially premelted. In correspondence with the experimental evidence surface premelting was demonstrated to be a reversible process. Surface

premelting was found to progress into the inner region of Au nanoparticles without a completely premelted surface.

Hu et al.[26] employed molecular dynamics simulation to investigate the rapid melting and subsequent cooling process of zinc oxide nanoparticles in liquid tetradecane upon picosecond laser heating. The radius of the nanoparticle varies from 10 to 30 $\mathring{A}$ which corresponds to the number of ZnO atoms ranging between 408 and 9456. The coalescence of two neighboring melted nanoparticles into a larger particle and the recrystallization of the latter upon cooling were studied. for nanosized particles in a liquid medium, the solidification temperature was far below the melting point, which was the sign of undercooling. The solidification temperature exhibited the same trend as the melting point when the particle size decreases. The difference between the melting and solidification temperatures was almost the same across the entire particle radii range studied. Joshi et al.[31] used molecular dynamics simulations to study melting of Ni and Fe nanoparticles with diameters in the range of 2-12nm. They obtained a linear relationship for melting temperature with the inverse of nanoparticle diameter. The simulations demonstrated that melting is surface initiated and that a finite temperature range exists in which partial melting of the nanoparticle occurs.

Sankarasubramanian and Kumar[58] studied the effect of surface anisotropy on the melting temperatures of free-standing gold nanofilms with thicknesses in the range of 1-40nm using molecular dynamics simulations. Among the films with low index crystallographic surfaces, those with 110 surface (least close-packed and highest surface energy) showed lowest melting temperatures whilst those with 111 surface (most close-packed and lowest surface energy) showed highest melting temperatures. Prolonged isothermal heat treatment demonstrated that there is no coexistence of equilibrium thickness of liquid layer with solid, in the case of free-standing nanofilm, below its melting temperature.

Shao et al.[59] investigated the structure, phase transition, and nucleation of Au nanoparticles with N = 467-2230 atoms, confined within armchair single-walled car-

bon nanotubes. The melting started from the innermost layer and freezing started from outermost layer for confined Au nanoparticles. Tang et al.[63] studied the melting behaviors of aluminum (111) perfect/nonperfect surfaces, characterized by structure ordering parameter. Al perfect surface had a superheating temperature above bulk Al melting point by about 80K. Al nonperfect surface had somewhat different local lattice structure from that on perfect surface. Al nonperfect surfaces tempt to premelt when temperature was less than melting temperature of bulk Al, in this simulation, by about 45K.

Phase field model

Sakai[57] used Landau theory for the melting of Sn nanoparticles and showed the nonlinear relationship between the melting point and the reciprocal of radius. He also showed that surface melting state becomes difficult to observe as particle radius decreases down to a critical value which was in contrast to the common belief that surface-induced melting becomes more dominant for smaller particles.

Chang and Johnson[10] presented an analytical solution to the two-parabola Landau model, applied to melting of metal particles with sizes in the nanoscale range. The liquid skin formation was found to occur only for particles with radii greater than an explicitly given critical radius. For particles with size comparable to the correlation length, a nonlinear dependence on size was found for both the melting temperature and the latent heat of fusion. For large systems compared to the correlation length, classical thermodynamic results was found.

Chernyshev[12, 13] determined the temperature of surface premelting in terms of the Landau mean field model. For the definition of the order parameter, the Lindemann criterion was employed, which states that crystal will melt when the root-mean-square displacement of the atoms in the crystal exceeds a certain fraction of the interatomic distance. It was shown that if the radius of a particle exceeds 10 nm approximately, the dependence of surface premelting temperature on size is weak.

Small particles

Small nanoparticles, usually less than 5nm in radius, experience different behavior in melting. Ercolessi et al.[20] predicted the existence of critical radius for Au nanoparticles using molecular dynamics simulations. They found that Au particles with R < 1 nm, do not experience quasi-liquid layer. Oshima and Takayanagi[44] observed pseudo-crystalline phase for tin clusters with R < 2.5nm. Clusters with 2.5 nm < R < 3.5nm were mainly observed to be crystalline while a small fraction were still in the pseudocrystalline phase.

Kofman et al.[33] showed that for Pb clusters of sizes smaller than 5nm, surface melting disappears and the melting process is discontinuous and the solid-liquid transition is sharp (no surface melting). Bachels et al.[3] experimentally obtained the critical radius of Sn to be 3.5nm. Chang and Johnson[10] concluded that the liquid skin formation as a precursor of melting, occurs only for particles with radii greater than a critical radius.

Alavi and Thompson[2] showed that aluminum nanoparticles smaller than 2.5nm show bistability between the solid and liquid phases. Nanoparticles larger than 2.5nm exhibited surface premelting behavior. Puri and Yang[51] showed that for Al particles with size less than 3nm, the solid and liquid phases coexist.

Wang et al.[66] showed that for Au nanoparticles with R > 1.22nm, surface is partially premelted. Chernyshev[13] showed that if the radius of a particle is less than 5 nm, the dependence of surface premelting temperature on size is strong. To define the critical radius below which surface melting does not occur, he deduced a relationship. For Al and Sn, the critical radius was 4.91nm and 3.83nm respectively. So it can be concluded that if the size of nanoparticles is less than the critical size, surface melting is not observed. For most materials, this critical radius is less than 5nm.

Thesis Organization

In chapter 2, phase field method coupled to mechanics is used to study premelting and melting of aluminum nanoparticles in the region of metastability and complete instability of solid and melt. Size dependence of melting temperature from this model is compared to experimental data where results are in better agreement than molecular dynamics results. In chapter 3, a deviatoric transformation strain is added to the model which promotes the driving force for phase transformation. In chapter 3, finite width of external surface layer is added to the phase field model to include transition between particle and gas at the surface. Barrierless and kinetic melting of aluminum particles are studied and bistability between solid and surface layer, and solid and melt is studied.

References

1. Ajayan, P.M. and Marks, L.D., Phys. Rev. Lett., 63(3), 279-282, 1989.

2. Alavi, S. and Thompson, D.L., J. Phys. Chem. A, 110, 1518-1523, 2006.

3. Bachels, T., Gntherodt, H.J. and Schfer, R., Phys. Rev. Lett., 85(6), 1250-1253, 2000.

4. Bal'makov, M.D., Glass Physics and Chemistry, 34(1), 110-112, 2008.

5. Blackman, M. and Curzon, A.E., Structure and Properties of Thin Film, (New York: Wiley), pp. 217-222, 1959.

6. Bockmon, B.S., Pantoya, M.L., Son, S.F., Asay, B.W. and Mang, J.T., J. Appl. Phys., 98, 064903, 2005.

7. Bruzostowski, T.A. and Glassman, I., in Heterogeneous Combustion, edited by H. G. Wolfhard, I. Glassman, and L. Green, Jr. Academic, New York, 1964.

8. Buffat, P. and Borel, J.P., Phys. Rev. A, 13(6), 2287-2298, 1976.

9. Castro, T., Reifenberger, R, Choi, E. and Andres, P., Phys. Rev. B., 42(13), 8548-8556, 1990.

10. Chang, J. and Johnson, E., Philos. Mag., 85(30), 3617-3627, 2005.

11. Chattopadhyay, K. and Goswami, R., Prog. in Mat. Sci., 42, 287-300, 1997.

12. Chernyshev, A.P., Mat. Chem. and Phys., 112, 226-229, 2008.

13. Chernyshev, A.P., Mat. Lett., 63, 1525-1527, 2009.

14. Chushak, Y.G. and Bartell, L.S., J. Phys. Chem. B, 105, 11605-11614, 2001.

15. Coombes, C.J., J. Phys., 2, 441-449, 1972.

16. Couchman, P.R., and Jesser, W. A., Nature, 269(6), 481-483, 1977.

17. Devaud, G. and Willens, R.H., Phys. Rev. Lett., 57(21), 2683-2685, 1986.

18. Dick, K., Dhanasekaran, T., Zhang, Z. and Meisel, D., J. Am. Chem. Soc., 124(10), 2312-2317, 2002.

19. Dippel, M., Maier, A., Gimple, V., Wider, H., Evenson, W.E., Rasera, R.L. and Schatz, G., Phys. Rev. Lett., 87(9), 095505, 2001.

20. Ercolessi, F., Andreoni, W. and Tosatti, E., Phys. Rev. Lett., 66(7), 911-914, 1991.

21. Eroshenko, Y.N., Usp. Fiz. Nauk, 173(12), Phys. Usp., 46(12), 2003.

22. Frenken, J.W.M. and van der Veen, J.F., Phys. Rev. Lett., 54(2), 134-137, 1985.

23. Gladkich, N.T., Niedermayer, R. and Spiegel, K., Phys. Stat. Solidi., 15, 1966.

24. Goswami, R. and Chattopadhyay, K., Acta Metall. Mater., 43, 2837-2847, 1995.

25. Granier, J.J. and Pantoya, M.L., Combust. Flame, 138, 373-383, 2004.

26. Hu, M., Poulikakos, D., Grigoropoulos, C.P. and Pan, H., J. Chem. Phys., 132, 164504, 2010.

27. Jesser, W.A., Shneck, R.Z. and Gile, W.W., Phys. Rev. B, 69, 144121, 2004.

28. Jiang, Q., Shi, H.X. and Zhao, M., J. Chem. Phys., 111(5), 2176-2180, 1999.

29. Jiang, Q., Yang, C.C. and Li, J.C., Macromol. Theo. Simul., 12(1), 57-60, 2003.

30. Johari, G.P., Philos. Mag. A, 77(6), 1367-1380, 1998.

31. Joshi, N.P., Spearot, D.E. and Bhat, D., J. Nanosci. Nanotech., 10, 5587-5593, 2010.

32. Kofman, R., Cheyssac, P., Aouaj, A., Lereah, Y., Deutscher, G.; Ben David, T., Penisson, J.M. and Bourret, A., Surf. Sci., 303, 231-246, 1994.

33. Kofman, R., Cheyssac, P., Lereah, Y. and Stella, A., Eur. Phys. J. D, 9, 581-584, 1999.

34. Lai, S.L., Guo, J.Y., Petrova, V., Ramanath, G. and Allen, L.H., Phys. Rev. Lett., 77(1), 99-102, 1996.

35. Lai, S.L., Carlsson J.R.A. and Allen, L.H., Appl. Phys. Lett., 72(9), 1098-1100, 1998.

36. Lereah, Y., Deutscher, G., Cheyssac, P. and Kofman, R., Europhys. Lett., 12, 709-713, 1990.

37. Levitas V.I., Asay, B.W., Son, S.F. and Pantoya, M., Appl. Phys. Lett., 89(7), 071909, 2006.

38. Levitas, V.I., Asay, B.W., Son, S.F. and Pantoya, M., J. Appl. Phys., 101, 083524, 2007.

39. Levitas, V.I., Pantoya, M.L. and Dikici, B., Appl. Phys. Lett. 91, 011921, 2008.

40. Levitas, V.I., Pantoya, M.L., Chauhan, G. and Rivero, I., J. Phys. Chem. C, 113, 14088-14096, 2009.

41. Levitas, V.I., Lee, D.W. and Preston, D.L., Int. J. Plast., 26(3), 395-422, 2010.

42. Lipowsky, R., Phys. Rev. Lett., 49, 1575-1578, 1982.

43. Mei, Q.S., Wang, S.C., Cong, H.T., Jin, Z.H. and Lu, K., Acta Materialia, 53, 1059-1066, 2005.

44. Oshima, Y. and Takayanagi, K., Zeit. Phys. D., 27, 287-294, 1993.

45. Nanda, K.K., Sahu, S.N. and Behera, S.N., Phys. Rev. A, 66, 013208, 2002.

46. Pantoya, M.L. and Granier, J.J., Propell. Explos. Pyrotech., 30, 53-62, 2005.

47. Park, K., Lee, D., Rai, A., Mukherjee, D. and Zachariah, M., J. Phys. Chem. B, 109, 7290-7299, 2005.

48. Pawlow, P., Z. phys. Chem., 65, 545-548, 1909.

49. Peters, K.F., Chung, Y.W. and Cohen, J.B., Appl. Phys. Lett. 71(16), 2391-2393, 1997.

50. Peters, K.F., Cohen, J.B. and Chung, Y.W., Phys. Rev. B, 57(21), 13430-13438, 1998.

51. Puri, P. and Yang, V., J. Phys. Chem. C., 111, 11776-11783, 2007.

52. Qi, W.H., Physica B, 368, 46-50, 2005.

53. Rie, E., Z. phys. Chem, 104, 354-362, 1923.

54. Reiss, H. and Wilson, I.B., J. Colloid Sci., 3, 551-561, 1948.

55. Ruan, C.Y., Murooka, Y., Raman, R.K. and Murdick, R.A., Nano Lett., 7(5), 1290-1296, 2007.

56. Safaei, A., Attarian Shandiz, M., Sanjabi, S. and Barber, Z.H., J. Phys. Cond. Matt., 19, 216216, 2007.

57. Sakai, H., Surf. Sci., 351, 285-291, 1996.

58. Sankarasubramanian, R. and Kumar, K., Comput. Mat. Sci., 49, 386-391, 2010.

59. Shao, J., Yang, C., Zhu, X. and Lu, X., J. Phys. Chem. C, 114(7), 2896-2902, 2010.

60. Sheng, H.W., Ren, G., Peng, L.M., Hu, Z.Q. and Lu, K., J. Mat. Res., 12(1), 119-123, 1997.

61. Sun, J. and Simon, S.L., Thermochim. Acta, 463, 32-40, 2007.

62. Takagi, M., J. Phys. Soc. Japan, 9, 359-363, 1954.

63. Tang, F.L., Cheng, X.G., Lu, W.J. and Yu, W.Y., Physica B, 405, 1248-1252, 2010.

64. Trunov, M.A., Umbrajkar, S.M., Schoenitz, M., Mang, J.T. and Dreizin, E.L., J. Phys. Chem. B., 110, 13094-13099, 2006.

65. Vanfleet, R.R. and Mochel, J.M., Surf. Sci., 341, 40-50, 1995.

66. Wang, N.Y., Rokhlin, S.I. and Farson, D.F., Nanotechnology, 19, 415701, 2008.

67. Wautelet, M., Eur. Phys. J. Appl. Phys., 29, 51-54, 2005.

68. Wronski. C.R.M., Br. J. Appl. Phys., 18, 1731-1737, 1967.

69. Wu, B., Tillman, P., McCue, S.W. and Hill, J.M., J. Nanosci. Nanotech., 9, 885-888, 2009.

70. Wu, B., McCue, S.W., Tillman, P. and Hill, J.M., Appl. Math. Modell., 33, 2349-2367, 2009.

71. Zhao, S.J., Wang, S.Q., Cheng, D.Y. and Ye, H.Q., J. Phys. Chem. B, 105, 12857-12860, 2001.

72. Zou, C.D., Gao, Y.L., Yang, B. and Zhai, Q.J., Trans. Nonferr. Met. Soc. China, 20, 248-253, 2010.

CHAPTER 2. SIZE AND MECHANICS EFFECTS IN SURFACE-INDUCED MELTING OF NANOPARTICLES

Modified from a paper published in the Nature Communications

Valery I. Levitas* and Kamran Samani †

Abstract

Various melting-related phenomena (like surface melting, size dependence of melting temperature, melting of few nm-size particles, and overheating at very fast heating rate) are of great fundamental and applied interest, although the corresponding theory is still lacking. Here we develop an advanced phase-field theory of melting coupled to mechanics, which resolves numerous existing contradictions and allowed us to reveal exciting features of melting problems. The necessity of introducing an unexpected concept, namely coherent solid-melt interface with uniaxial transformation strain, is demonstrated. A crossover in temperature dependence of interface energy for radii below 20 nm is found. Surface-induced pre-melting and barrierless melt nucleation for nanoparticles down to 1 nm radius have been studied, and the importance of advanced mechanics is demonstrated. Our model describes well experimental data on the width of the molten layer versus temperature for the Al plane surface and on melting temperature versus particle radius.

*Iowa State University, Departments of Aerospace Engineering, Mechanical Engineering, and Material Science and Engineering, Ames, Iowa 50011, U.S.A.

†Iowa State University, Department of Mechanical Engineering, Ames, Iowa 50011, U.S.A.

Introduction

Numerous melting-related phenomena represent fundamental material problems and are currently under intense experimental and theoretical study. They include surface premelting and melting below the thermodynamic melting temperature θ_e, caused by reduction in surface energy and leading to appearance of a molten, nanometer-thick layer [1, 2]; reduction in melting temperature θ_m with reduction of the particle radius R down to nanoscale[3, 4]; melting of particles with radii comparable to and smaller than the equilibrium solid-liquid interface width δ_e, which is a few nm[3, 5]; and overheating above θ_e during very fast heating[6, 7]. All of these phenomena allow one to determine properties of solid and liquid deeply in the region of their metastability and even complete instability (i.e. above the solid instability temperature θ_i or below the melt instability temperature θ_c, see Supplementary Fig. 9), and to study intermediate states, various scale effects, and non-equilibrium thermodynamic and kinetic properties. These studies also have important applied aspects, e.g., for combustion of Al nanoparticles[8] that are the most known representatives of nanoenergetic materials. However, a consistent theoretical framework for the description of the above phenomena is lacking. The sharp-interface approach [9] (SIA) is not justified for the above problems. While there are important molecular dynamics (MD) studies[5, 6, 10], we focus on the continuum phase-field approach (PFA), which allows consideration of larger spatial and time scales and operates explicitly with thermodynamic and kinetic parameters determined at the macroscale (see Supplementary Discussion). When mechanics is taken into account, a basic problem of the description of finite-width, solid-liquid interface appears. Traditionally, solids and liquids are described in completely different continuum mechanical frameworks (e.g., solids are

described in undeformed states, while liquids are described in a deformed state), which sophisticates the description of intermediate state. Some works consider solid as very viscous liquid[13], i.e., neglect elastic shear modulus μ. Such a liquid-liquid interface is incoherent and does not generate internal elastic stresses, similar to sharp interface (Fig. 1). Alternatively[14], solid-melt interface is considered as a coherent interface (Fig. 1), in which shear modulus varies from that for solid to zero, and this results in generation of internal elastic stresses at the interface. When particle size is comparable to or smaller than the interface width, a coherent interface is the only reasonable choice. While this model is supposed to be more precise, the surface tension in it is not consistent with sharp-interface limit, even if $\mu = 0$. Also, even for liquid-liquid interface, expression for surface tension in PFA differs by a hydrostatic pressure from that in SIA[11–13]. This is a fundamental thermodynamic inconsistency, which is especially important for nanoscale interface radii.

Surface pre-melting and melting were studied using PFA[15–17] without involving mechanics. However, the employed equation for surface energy $\gamma(\eta) = a + b\eta^2$ did not allow homogeneous solution for solid ($\eta = 1$) (Fig. 2), exhibiting a surface disordered structure even below melt instability temperature θ_c, when the energy minimum corresponding to melt does not exist. Such an inconsistency also exhibits itself in unphysical regions in the phase diagram[15].

The goal of this paper is to develop a unified PFA coupled to mechanics and reveal nontrivial features of the above melt-related phenomena. Thus, a model with *coherent* solid-melt interface is developed (see Fig. 1), in which shear modulus μ varies from that for solid to zero, and this results in generation of internal elastic stresses at the interface. Thermodynamic potential in this model results in surface tension stresses consistent with the SIA, in contrast to known models with incoherent interface (for which $\mu = 0$)[11, 12, 13] and coherent interface[14]. Also, the necessity of introducing a non-spherical transformation strain, which in addition to volumetric expansion during

melting describes change in shape, is demonstrated. Our model resolves fundamental thermodynamic inconsistency and includes more advanced mechanics, which is especially important for nanoparticles. Also, a model for surface energy that varies during melting is developed, which resolves the aforementioned non-physical effects in existing models [15, 16, 17] and adds to them mechanics.

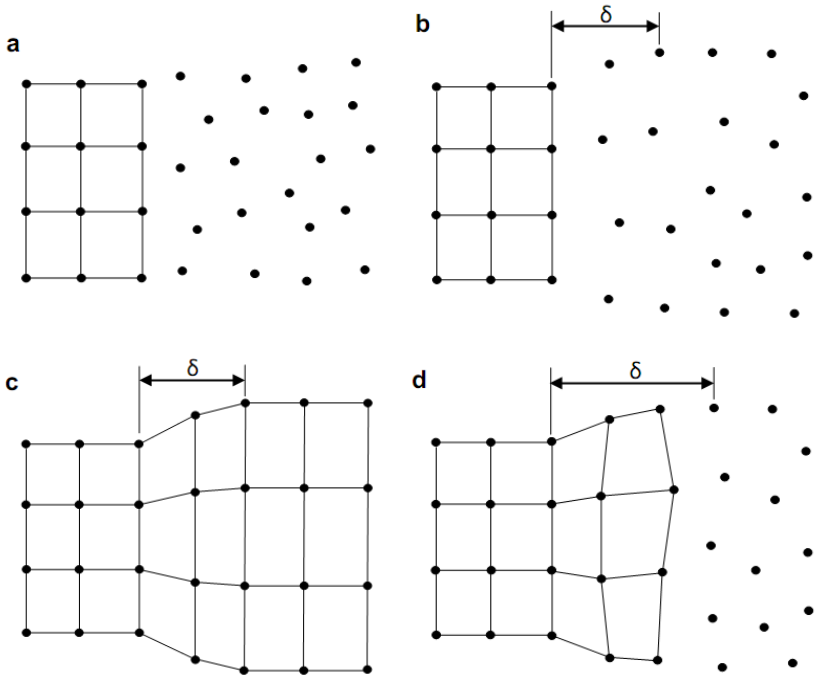

Figure 2.1 Different types of interfaces between solid and molten phases. (a) Traditional sharp incoherent solid-melt interface, which does not generate internal elastic stresses. (b) Incoherent, finite-width, solid-melt interface with zero shear modulus $\mu = 0$ that does not generate internal elastic stresses. (c) Coherent finite-width interface between two solid phases. Continuity of crystal lattice across the interface along with a change in the size of one of the lattices during transformation (due to transformation strain tensor $\boldsymbol{\varepsilon}_t$) generates internal elastic stresses. (d) Coherent, finite-width, solid-melt interface with nonzero shear modulus $\mu \neq 0$ that generates internal elastic stresses.

It is demonstrated that our model describes well experimental data on the width of the molten layer vs. temperature for the Al plane surface, and then it is applied to surface-induced pre-melting and barrierless melt nucleation for nanoparticles. It also describes well experimental data on θ_m vs. R, even better than MD simulations[5]. Then,

non-equilibrium and small-scale regimes were treated, i.e., interface profile, width, energy, and velocity have been determined and analyzed vs. R, interface position r_i, and large overheating and heating rates h. Thus, the derived analytical expression for interface velocity v describes well simulation results well outside of an expected range, namely even for $\theta > \theta_i$, h up to $10^{13}K/s$, and $r_i \geq 2\delta_e$. It also describes well the effect of large compressive and tensile pressure. Homogeneous melt nucleation competes for $h = 10^{13}K/s$ with interface propagation. For $R = 1$ and $3nm$, premelting occurs in the entire particle rather than at the surface only. Allowing for mechanics increases melting temperature by $70K$ for $R = 1nm$ particle due to pressure induced by surface tension. For $R \leq 1.5nm$, $\theta_m < \theta_c$, i.e., the particle melts more than $200K$ below θ_e while there is no local energy minimum corresponding to melt. While for a liquid-liquid interface our calculations reproduce the Laplace relationship for jump in radial stresses $\Delta\sigma_r$, for coherent solid-melt interface, $\Delta\sigma_r$ does not follow the Laplace relationship and even may possess the opposite sign, causing tension in the solid core instead of compression. Interface energy varies in a nontrivial way for $r_i \leq 4\delta_e \simeq 12nm$ with decreasing r_i, increasing for $\theta > \theta_e$ and decreasing for $\theta < \theta_e$; this is opposite to the behavior for $r_i > 12nm$.

Theory

We designate contractions of tensors $\boldsymbol{A} = \{A_{ij}\}$ and $\boldsymbol{B} = \{B_{ji}\}$ over one and two indices as $\boldsymbol{A}\cdot\boldsymbol{B} = \{A_{ij}\,B_{jk}\}$ and $\boldsymbol{A}:\boldsymbol{B} = A_{ij}\,B_{ji}$, respectively. The subscript $*$ means symmetrization; the subscripts or superscripts e, θ, and t are for elastic, thermal and transformational contributions to strain and energy; $\boldsymbol{I}$ is the unit tensor; $\Delta A = A_s - A_m$ for any property A, with subscripts s and m for solid and melt; $\overset{\circ}{\boldsymbol{\nabla}}$ and $\boldsymbol{\nabla}$ are the gradient operators in the undeformed and deformed states; and $\otimes$ designates a dyadic product.

To develop a unified approach to solid and liquid, we will consider liquid as the limit

case of isotropic viscoelastic solid with $\mu = 0$. For simplicity, viscosity is neglected, isothermal processes are considered, and shear strain is small. However, even if volumetric strain ε_0 is small, in order to reproduce surface tension one has to use fully large-strain formulation (see below). We will modify our recently developed theory of martensitic transformations in solids[18, 19] to describe melting. The Helmholtz free energy per unit undeformed volume of solid $\psi = \psi(\boldsymbol{\varepsilon}, \eta, \boldsymbol{\nabla}\eta, \theta)$, where $\boldsymbol{\varepsilon}$ is the strain tensor and η is the order parameter that varies from 1 in solid to 0 in melt. Using an irreversible thermodynamic procedure based on the application of the first and second laws of thermodynamics to the system with energy depending on the gradient of the order parameter (see[12] and references in it) and assuming linear relation between thermodynamic force and flux, one obtains expression for the stress tensor $\boldsymbol{\sigma}$ and the Ginzburg-Landau (GL) equation:

$$\boldsymbol{\sigma} = \frac{\partial \psi}{\partial \boldsymbol{\varepsilon}} - J^{-1}\left(\boldsymbol{\nabla}\eta \otimes \frac{\partial \psi}{\partial \boldsymbol{\nabla}\eta}\right)_*, \quad \frac{1}{\chi}\frac{\partial \eta}{\partial t} = -J^{-1}\frac{\partial \psi}{\partial \eta}|_{\boldsymbol{\varepsilon}} + \boldsymbol{\nabla}\cdot\left(J^{-1}\frac{\partial \psi}{\partial \boldsymbol{\nabla}\eta}\right), \tag{1}$$

$$J = \frac{\rho_0}{\rho} = 1 + \varepsilon_0 \tag{2}$$

where ρ_0 and ρ are the mass densities in the nondeformed and deformed states, χ is the kinetic coefficient, and $\boldsymbol{\varepsilon} = const$ while evaluating $\partial\psi/\partial\eta$. Kinematics relationships between displacement $\boldsymbol{u}$ and strain $\boldsymbol{\varepsilon} = 1/3\varepsilon_0\boldsymbol{I} + \boldsymbol{e}$, decomposition of $\boldsymbol{\varepsilon}$ and the equilibrium equation are

$$\boldsymbol{\varepsilon} = (\overset{\circ}{\boldsymbol{\nabla}}\,\boldsymbol{u})_*, \quad \boldsymbol{\varepsilon} = \boldsymbol{\varepsilon}_e + \boldsymbol{\varepsilon}_t + \boldsymbol{\varepsilon}_\theta, \quad \boldsymbol{\nabla}\cdot\boldsymbol{\sigma} = 0, \tag{3}$$

where $\boldsymbol{e}$ is the deviatoric strain. Energies and strains are defined as follows:

$$\psi = \psi^e(\varepsilon_0, \boldsymbol{e}, \eta, \theta) + J\breve{\psi}^\theta + \psi^\theta + J\psi^\nabla;$$

$$\psi^e = 0.5(K_m + \Delta K\phi(\eta))\varepsilon_{0e}^2 + 0.5\mu\phi(\eta)\boldsymbol{e}_e\boldsymbol{:}\boldsymbol{e}_e; \quad \psi^\theta = H(\theta/\theta_e - 1)\phi(\eta);$$

$$\breve{\psi}^\theta = A\eta^2(1-\eta)^2; \quad \psi^\nabla = 0.5\beta|\boldsymbol{\nabla}\eta|^2; \quad A := 3H(1-\theta_c/\theta_e); \tag{4}$$

$$\boldsymbol{\varepsilon}_t = \bar{\boldsymbol{\varepsilon}}_t(1-\phi(\eta)); \quad \boldsymbol{\varepsilon}_\theta = (\alpha_m + \Delta\alpha\phi(\eta))(\theta - \theta_e))\boldsymbol{I}; \quad \phi(\eta) = \eta^2(3-2\eta). \tag{5}$$

Here, K is the bulk modulus, β and α are the gradient energy and linear thermal expansion coefficients, H is the heat of fusion, $\breve{\psi}^\theta$ is the double well energy, and $\bar{\boldsymbol{\varepsilon}}_t$ is the

transformation strain that transforms the elemental volume of solid to melt under $\boldsymbol{\sigma} = 0$. While for martensitic phase transformations $\bar{\boldsymbol{\varepsilon}}_t$ is a tensor connecting two crystal lattices, for melting it is always pure volumetric strain, $\bar{\boldsymbol{\varepsilon}}_t = 1/3\varepsilon_{0t}\boldsymbol{I}$ [14, 11, 12, 13, 9]. We will show that the usual assumption causes very high internal stresses and elastic energy within interface, which suppresses melt nucleation and contradicts to experiment. Development of a complete theory for $\bar{\boldsymbol{\varepsilon}}_t$ is not a goal of this letter, but we consider an alternative expression for uniaxial $\bar{\boldsymbol{\varepsilon}}_t = \varepsilon_{0t}\boldsymbol{k} \otimes \boldsymbol{k}$, where $\boldsymbol{k} = \boldsymbol{\nabla}\eta/|\boldsymbol{\nabla}\eta|$ is the unit normal to the interface. In this case, the component of transformation strain along the interface is absent, which minimizes internal stresses and their energy. Then Eq.(2) looks like

$$\boldsymbol{\sigma} = \boldsymbol{\sigma}_e + \boldsymbol{\sigma}_{st}; \quad \boldsymbol{\sigma}_{st} = (\psi^{\nabla} + \breve{\psi}_\theta)\boldsymbol{I} - \beta\boldsymbol{\nabla}\eta \otimes \boldsymbol{\nabla}\eta; \tag{6}$$

$$\boldsymbol{\sigma}_e = (K_m + \Delta K\phi(\eta))\varepsilon_{0e} + \mu\phi(\eta)\boldsymbol{e}_e; \tag{7}$$

$$\frac{1}{\chi}\frac{\partial\eta}{\partial t} = \beta\nabla^2\eta - 6J^{-1}[H\left(\frac{\theta}{\theta_e} - 1\right) + \sigma^e\varepsilon_{0t} - 3p_e\Delta\alpha(\theta - \theta_e) + \frac{1}{2}\Delta K\varepsilon_{0e}^2 + \frac{1}{2}\mu\boldsymbol{e}_e\!:\!\boldsymbol{e}_e]\eta(1-\eta)$$
$$-4A\eta(1-\eta)(0.5-\eta); \quad 3p_e := \boldsymbol{\sigma}_e\!:\!\bar{\boldsymbol{I}}, \tag{8}$$

where $\boldsymbol{\sigma}_e$ and $\boldsymbol{\sigma}_{st}$ are the elastic stress and surface tension, $\sigma^e = p_e$ for volumetric transformation strain and $\sigma^e = \boldsymbol{k} \cdot \boldsymbol{\sigma}_e \cdot \boldsymbol{k}$ for uniaxial transformation strain. For a phase-equilibrium condition in the stress-free case, $\frac{\beta}{2}|\boldsymbol{\nabla}\eta|^2 = \breve{\psi}_\theta$ [20], and we have $\boldsymbol{\sigma}_{st} = \beta|\boldsymbol{\nabla}\eta|^2(\bar{\boldsymbol{I}} - \boldsymbol{k} \otimes \boldsymbol{k})$, i.e., it represents two equal normal stresses along the interface. Thus, $\boldsymbol{\sigma}_{st}$ is consistent with the SIA, unlike previous approaches [14, 11, 12, 13], which resolves a long-standing problem in PFA for melting.

In contrast to previous works on melting and other transformations in solids [14, 18], the gradient operator $\boldsymbol{\nabla}$ with respect to the deformed state was used, and the finite-strain factor J was included in the proper places. While use of $\boldsymbol{\nabla}$ is natural for liquids [11, 12, 13], this is not the case for solids. One of the unexpected points is that even for small strains, one cannot assume that $J \simeq 1$ and $\boldsymbol{\nabla} \simeq \overset{\circ}{\boldsymbol{\nabla}}$, because this leads to zero surface tension. The same thermodynamic procedure [19] that led to Eq.(2) also results in the boundary

conditions

$$J\frac{\partial\psi}{\partial\boldsymbol{\nabla}\eta}\cdot\boldsymbol{n}=\beta\nabla\eta\cdot\boldsymbol{n}=-\frac{d\gamma}{d\eta},\quad \sigma_n=\frac{2\gamma(\eta)}{R}+\bar{p}, \tag{9}$$

where $\boldsymbol{n}$ is the unit normal to the boundary, σ_n is the normal to interface stress, $1/R$ is the mean curvature, and $\bar{p}$ is the external pressure. Eq.(7) represents a generalization for the 3-D case and coupling with mechanics of known condition[16, 15]. We require the following properties of the surface energy: $\gamma(0)=\gamma_l$; $\gamma(1)=\gamma_s$; $\frac{d\gamma(0)}{d\eta}=\frac{d\gamma(1)}{d\eta}=0$. The last equation guaranties that homogeneous melt $\eta=0$ and solid $\eta=1$ satisfy Eq.(7) and removes contradiction in the known papers[16, 15] (see Fig. 2). These properties are met for polynomial $\gamma(\eta)=\gamma_l+\Delta\gamma(a\eta^2+(4-2a)\,\eta^3+(a-3)\eta^4)$ of the lowest degree with a parameter a.

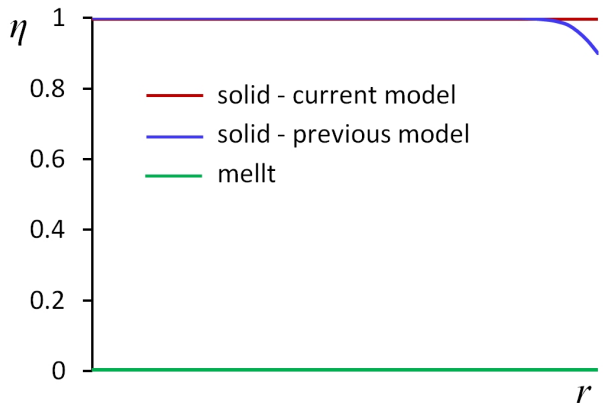

Figure 2.2 Stationary solutions for Ginzburg-Landau equation with different models for surface energy. Previous models[15, 16, 17] (blue line) did not allow a homogeneous solution for the solid ($\eta=1$), exhibiting a surface disordered structure at any temperature. Our model Eq.(8) (red line) is developed using the condition that it allows a homogeneous solution for the solid. The green line represents melt ($\eta=0$).

One can demonstrate that a criterion of barrierless surface-induced melt nucleation is consistent with a sharp-interface condition, $\Delta\gamma>\gamma_{s-l}$, when $a=3$. Then $\gamma(\eta)=\gamma_l+\Delta\gamma\phi(\eta)$. If surface energy does not change during melting, then $\gamma=const$ and Eq.(7) reduces to traditional boundary condition $\nabla\eta\cdot\boldsymbol{n}=0$.

We focus on Al nanoparticles; material parameters are given in Supplementary Discussion. In particular, $\theta_e = 933.67K$, $\theta_c = 0.8\theta_e = 746.9K$, and $\theta_i = 1.2\theta_e = 1120.4K$, $\delta_e = 2.97nm$. Note that all material parameters have been obtained for a macroscopic sample with no fitting parameters left. None of our developments (coherent interface with uniaxial transformation strain, expressions for free energy that results in correct expression for surface tension, and expression for surface energy) require additional material parameters.

Results

First, homogeneous heating of particles of radius R was considered and stationary solutions were found for each temperature. The thickness h of pre-molten and completely molten surface layer (determined by an interphase radius r_i, i.e., by point with $\eta = 0.5$) have been plotted vs. $\theta_e - \theta$ (Fig. 3). At melting temperature, θ_m, the stationary, two-phase solution ceases to exist and interface propagates to the center.

Size-dependence of melting temperature

In Fig. 4, the lowest curve is for GL equation only, i.e. for neglected mechanics. Below radius $R^* = 6.12nm$, results for volumetric $\boldsymbol{\varepsilon}_t$ give slightly lower θ_m and are closer to experimental points, while for $R > R^*$ results for uniaxial $\boldsymbol{\varepsilon}_t$ are much lower. For $R > 21.2nm$ and volumetric $\boldsymbol{\varepsilon}_t$, $\theta_m > \theta_e$. This is in contrast to experiments for flat interface, for which $\theta_m = \theta_e$. That is why uniaxial transformation strain was used, in contrast to known models[11, 12, 13]. For neglected mechanics and for uniaxial $\boldsymbol{\varepsilon}_t$ melting temperature tends to θ_e for infinite radius. Experimental points are between curves with neglected mechanics and for uniaxial $\boldsymbol{\varepsilon}_t$ for $R > R^*$ and for volumetric $\boldsymbol{\varepsilon}_t$ for $R < R^*$.

Coupling with mechanics for $2 - 3nm$ particles increases melting temperature by $30 - 40K$ (see also Fig. 5) and makes it closer to the experiments. Surprisingly, our results are in better correspondence with experiments than known MD approaches (Fig.

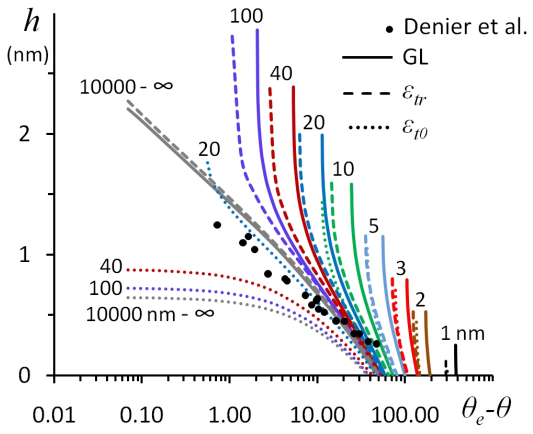

Figure 2.3 Thickness of molten surface layer versus temperature for different particle radii. Each color represents a particle radius shown in nm near curves. Solid lines are results of GL model without mechanics. Dotted and dashed lines are obtained for coupled GL and mechanics model with volumetric and uniaxial transformation strains, respectively. Black dots are experimental data[1] obtained using medium energy ion scattering. Experimental points for a plane surface are close to the calculations for infinite radius for GL and coupled models with uniaxial transformation strain. All curves, excluding those interrupted at $0.1K$, are ended at the melting temperature.

4b). Thus, we can conclude that the model of coherent solid-melt interface has good potential for the description of experiments; traditional volumetric $\boldsymbol{\varepsilon}_t$ is not adequate for large particles, i.e., there is interface restructuring, driven by the internal stress relaxation; and a thermodynamic and kinetic theory for $\boldsymbol{e}_t$ should be developed.

Surface pre-melting and melting

As shown in Fig. 3, for plane interface ($R \to \infty$), plots for thickness of the molten layer vs. θ for GL and uniaxial $\boldsymbol{\varepsilon}_t$ almost coincide and are very close to experimental points, which justifies validity of our model for surface energy.

Results for volumetric $\boldsymbol{\varepsilon}_t$ are inconsistent with experiments. For nanoparticles, $h(\theta)$ plots consist of two parts: an almost straight line with small slope at high temperature with transition to an almost vertical line for temperatures close to θ_m. The maximum thickness of the molten layer is very close for the GL model and the model with uniaxial

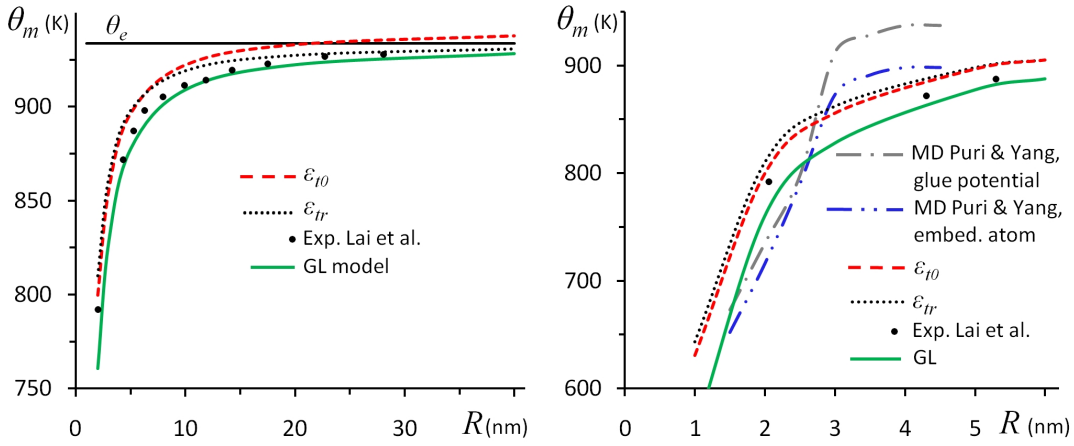

Figure 2.4 Melting temperature of Al versus particle radius. (a) Curves are calculated using three models: GL equations only (GL, green line), GL equation coupled to mechanics with volumetric (ε_{t0}) (red line) and uniaxial (ε_{tr}) (black dotted line) transformation strain. Dots are experimental data from[3] obtained using thin-film differential scanning calorimetry. The horizontal line is the equilibrium temperature (the same curve designations are used in Fig. 4(b)). (b) Molecular dynamics results are added for particles with radii in the 1-6 nm range. Gray and blue lines are MD results[5] using glue and embedded atom potentials, respectively.

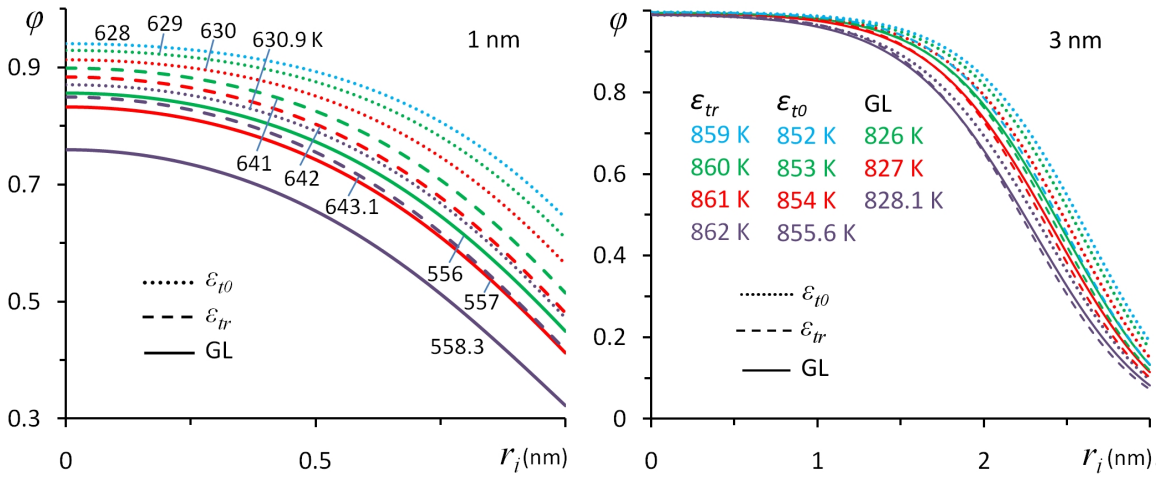

Figure 2.5 Stationary interface profiles $\phi(\eta)$ for Al particles for different temperatures. (a) $R = 1nm$; (b) $R = 3nm$. Solid lines are the results obtained with the GL model. Dotted and dashed lines are obtained using coupled GL and mechanics models with volumetric and uniaxial transformation strains, respectively. Different temperatures are considered for each model, which are designated on the graphs. The lowest curve for each model corresponds to the melting temperature.

$\boldsymbol{\varepsilon}_t$. While curves for these models look also close, for some temperatures the difference in thickness is by a factor of two or larger. For $R \leq 5nm$, curves for volumetric and uniaxial $\boldsymbol{\varepsilon}_t$ are very close.

Stationary distributions of interface profiles $\phi(\eta)$ (note that $\phi(\eta)$ rather than η describes the variation of all properties, see Eq.(2)) in particles of $R = 1$ and $3nm$ are presented in Fig. 5. For all cases, the complete liquid phase ($\eta = 0$) is not reached. For 1 and $3nm$, stationary premelting (i.e. $\phi(\eta) < 1$) occurs in the entire particle rather than at the surface only. Allowing for mechanics increases melting temperature by $70K$ for $R = 1nm$ particle, mostly due to pressure induced by surface tension. Note that for $R < 1.5nm$, one has $\theta_m < \theta_c$, i.e., particle melts even when bulk melt is unstable.

Surface tension

Distributions of radial stresses along r are shown in Fig. 6. When internal elastic stresses can be neglected (for equal thermoelastic properties of phases and $\mu = 0$, i.e., for liquid-liquid transformation, or for $\boldsymbol{\varepsilon}_t = 0$), our calculations at θ_e reproduce the Laplace relationship for jump in radial stresses $\Delta\sigma_r = -2\gamma_{s-l}/r_i$ within the error of 0.14% for $r_i > 11nm$ and 1.03% at $r_i = 5nm$. For actual solid-melt properties and volumetric $\boldsymbol{\varepsilon}_t$, $\Delta\sigma_r$ does not follow the Laplace relationship and even possesses the opposite sign, causing tension in the solid core (Fig. 6). For uniaxial $\boldsymbol{\varepsilon}_t$, $\Delta\sigma_r = -k2\gamma_{s-l}/r_i$ with $k > 1$.

Interface profile and energy

For plane interface, $\theta = \theta_e$, and neglected mechanics, the GL equation allows analytical solution for an equilibrium interface:

$$\eta_e = [1 + \exp(5.54x/\delta_e)]^{-1}; \quad \delta_e = 5.54\sqrt{\beta/(2A)}; \quad \gamma_{s-l} = \sqrt{\beta A/18}, \tag{10}$$

where the interface width is $\delta = |r_l - r_s|$ and r_l and r_s are determined from the conditions $\phi(\eta) = 0.01$ and 0.99, respectively. Surface energy in non-equilibrium state γ^n_{s-l} is

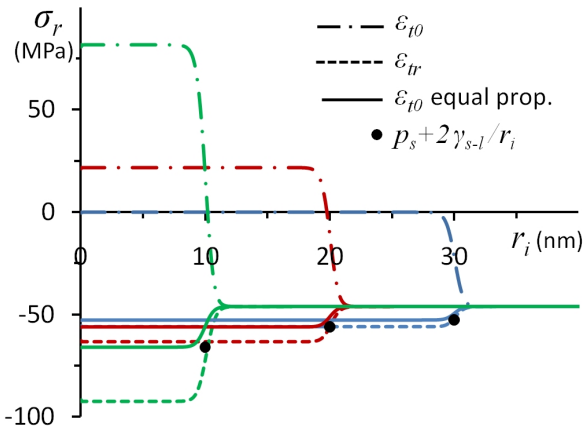

Figure 2.6 Distribution of radial stresses for three interface positions. The blue line corresponds to the interface radius at 30nm, the red at 20nm, and the green at 10nm. Distributions are calculated at θ_e using models with volumetric (ε_{t0}) (dotted line) and uniaxial (ε_{tr}) (dashed line) transformation strains, as well as with equal thermoelastic properties of solid and melt (solid line), i.e. for liquid-liquid transformation. Dots designate pressures in melt $p_s + 2\gamma_{s-l}/r_i$ based on the Laplace equation that coincides with results of calculations for equal thermoelastic properties of the solid and melt.

defined as an excess energy with respect to solid (where $0.5 < \eta \leq 1$) and liquid (where $0 \leq \eta \leq 0.5$)

$$\gamma^n_{s-l} = \left(\int_0^{r_i} (\rho\psi - \rho_s\psi_s) r^2 dr + \int_{r_i}^{R-h} (\rho\psi - \rho_l\psi_l) r^2 dr \right) / r_i^2. \tag{11}$$

With neglected mechanics, interface width is described by Eq.(10) within 2.5% error for $r_i \geq 2\delta_e$ and $\theta \leq 1.25\theta_e$, i.e., even above θ_i. For $r_i = 2nm$, $\delta = 3.99nm = 1.34\delta_e$. Mechanics slightly ($< 1\%$) increases the width for $\theta = \theta_e$, but this difference grows with increasing temperature; e.g., δ =3.03 and 3.06 nm for $r_i = 30nm$, $\theta = 1.2\theta_e$ and $1.25\theta_e$, respectively. Still, the interface profile differs from Eq.(10) within $\Delta\phi = 0.03$ error for $r_i \geq \delta_e/2$ and $\theta \leq \theta_i$. Interface energy γ^n_{s-l} vs. interface radius for different temperatures is shown in Fig. 7. For equilibrium temperature, interface energy starts growing for $r_i < 10nm$ and maximum deviation from $\gamma_{s-l} = 0.1J/m^2$ is 11.2% for the smallest $r_i = 2.41nm$, for which full interface exists. For $r_i > 20nm$ expected decrease in γ^n_{s-l} with growing temperature is observed. For $r_i < 20nm$, unexpected

opposite relation is found, which means change in sign of the interface entropy. Note that for $r_i > 4\delta_e \simeq 12nm$, deviation of γ^n_{s-l} from γ_{s-l} does not exceed 3% in the entire temperature range $\theta_c < \theta < \theta_i$, which is well below of inaccuracy of experimental data for interface energy.

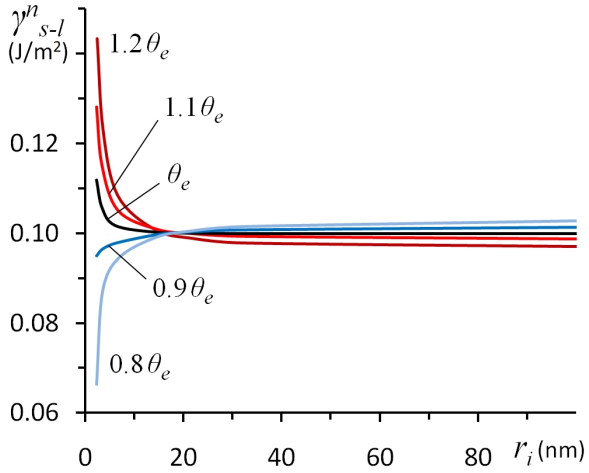

Figure 2.7 Non-equilibrium interface energy γ^n_{s-l} versus interface radius for different temperatures. Results are obtained for both volumetric and uniaxial transformation strains and practically coincide. At the position of $r_i = 10nm$, curves from top to bottom correspond to temperatures of $1.2\theta_e$, $1.1\theta_e$, θ_e, $0.9\theta_e$ and $0.8\theta_e$. A crossover in temperature dependence of interface energy for radii below 20 nm is evident.

Interface velocity

When internal stresses inside an interface are neglected, the following linear relationship is obtained for $r_i \gg \delta_e$ between interface velocity v_0 and the thermodynamic force for interface propagation per unit deformed volume of solid X:

$$\begin{aligned} v_0 &= 6X\chi\sqrt{\beta\rho_m/(2A\rho_s)}, \\ X &= \frac{\rho_s}{\rho_{0s}}H\left(1-\frac{\theta}{\theta_e}\right)+p_m\left(\frac{\rho_s}{\rho_m}-1\right)-\frac{1}{2}\left(\frac{p_m^2}{K_m}-\frac{p_s^2}{K_s}\right)+\frac{2\gamma_{s-l}}{r_i}. \end{aligned} \qquad (12)$$

It can be seen from Fig. 8, that Eq.(8) describes well (error $\leq$ 3%) results of our simulations even for $r_i > 2\delta_e$ for neglected internal stresses and for heating rates as high as $10^{13}K/s$. Due to small particle size, homogeneous temperature is assumed, see analytical

justification in[8]. The temperature at some points in Fig. 8 significantly exceeds the instability temperature θ_i and reaches $1344K$ for $10^{13}K/s$; that is why interface does not reach the center of the particle, because homogeneous reduction of η in the central part completes melting faster. Even for high compressive and tensile pressures, Eq.(8) works well when internal stresses are negligible: for external pressure $p = 4GPa$ and $\theta = 1225K$ deviations from simulations for $r_i = 30$ and $20nm$ are within 2.14% and for $p = -4GPa$ and $\theta = 750K$ it is within 1.05%. Velocities for volumetric $\boldsymbol{\varepsilon}_t$ are higher, and for uniaxial $\boldsymbol{\varepsilon}_t$ they are lower than for the case with $\mu = 0$.

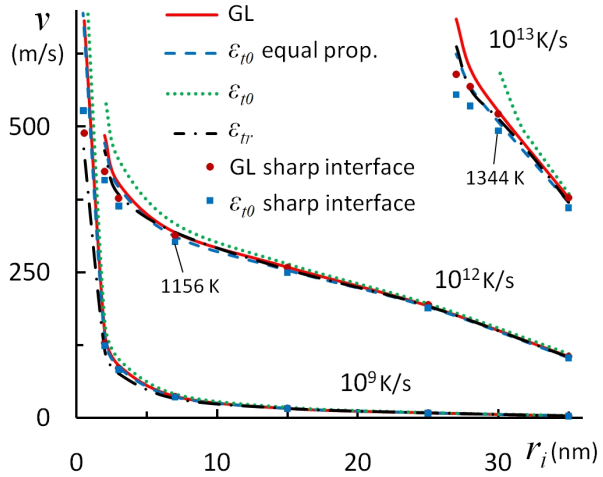

Figure 2.8 Interface velocity versus position for three heating rates. The heating rate is $10^9K/s$ at the bottom, $10^{12}K/s$ in the middle, and $10^{13}K/s$ at the top. Curves correspond to PFA with different models (red line for GL model, green and black lines for models with volumetric and uniaxial transformation strains, respectively, and blue line for volumetric transformation strain with equal solid and melt properties). Points correspond to SIA, namely to Eq.(8).

Discussion

Note that the SIA[21] to melting/solidification at the nanoscale, which includes surface-induced melting and coupled to mechanics, can be applied to our problems down to some

radius, which is to be determined by comparison with PFA. However, when the interface region is a significant part of the particle, PFA is more precise and does not require any adjustments. In contrast, SIA should incorporate the size-dependence of surface melting (Fig. 3), size- and temperature-dependence of surface energy (Fig. 7), and surface stresses not equal to surface tension (Fig. 6). To summarize, an advanced phase-field approach to pre-melting and melting coupled to mechanics is developed. It is applied to study melting deeply in the region of metastability and complete instability of solid and melt, intermediate states at the surface and in few nm-size particles, scale effect, and non-equilibrium thermodynamic and kinetic properties. The importance of mechanics effects (even without external pressure) is elucidated. Crossover in temperature dependence of the interface energy for radii below $20nm$ and violation of the Laplace relationship for the jump in pressure is obtained. Conceptual validity of the coherent solid-melt is proven and necessity for its further development, namely formulation of the evolution equation for the deviatoric part of $\boldsymbol{\varepsilon}_t$, is demonstrated.

Methods

15 to 30 elements per interface width and an adaptive time step with a minimum of 1000 time steps for a typical nonstationary problem are used. To check the model, interface profiles are compared to analytical results for plane interface at equilibrium temperature[22]. Even with interface radius of 30nm, difference between planar analytical solution and COMSOL GL result is less than 0.1%. Also the solid-liquid interface energy in Al practically coincides with its analytical value of $0.1 J/m^2$, see Fig. 7.

Supplementary Discussion

Short review of existing approaches and problems

There are two main continuum methods of studying melting: (a) the sharp-interface approach[9] (SIA) with jump of thermodynamic parameters across an interface with $\delta = 0$,

and (b) the phase-field approach (PFA), in which melting is described by continuous variation of an order parameter η from 1 to 0 across the interface of finite width δ[11–17]; all other thermodynamics parameters are continuous across an interface as well. The evolution of η is described by Ginzburg-Landau (GL) or phase-field equation, which represents the linear relationship between $\dot{\eta}$ and conjugate thermodynamic force X. The PFA is more detailed than the SIA but requires more advanced thermodynamic potential that describes intermediate states between solid and liquid in terms of the order parameter η (figure 9) and interface energy in terms of gradient $\nabla\eta$. One of the requirements for PFA is that for the sample size $L/\delta \gg 1$, equations of PFA should transform to those of SIA. This is, however, not the case in known publications for surface tension, because expressions for surface tension in both approaches differ by a hydrostatic pressure[11,13]. This is a fundamental thermodynamic inconsistency, which is especially important for nanoscale interface radii. In the paper, we find expression for thermodynamic potential for PFA, which results in consistent expression for surface tension, and we derive the kinetic relationship for interface velocity, v, for $L/\delta \gg 1$, i.e., $v_0(X)$.

For nanoparticles and solid-liquid interface radii r_i that are comparable with interface width δ, SIA fails and PFA is the only reliable continuum approach. It is expected that interface energy may depend on the interface radius and that the interface velocity v may deviate from the kinetic relationship $v_0(X)$ obtained for $\tilde{r} = r/\delta \gg 1$. SIA also fails when nanoparticles are overheated fast to temperature θ close or even above the crystal lattice instability temperature θ_i, at which energy minimum corresponding to solid disappears (supplementary figure 1). One of our goals is to study numerically these non-equilibrium and small-scale regimes, i.e., determine and analyze interface profile, width, energy, and velocity.

Material parameters for aluminum

We will focus on Al nanoparticles and use the following material parameters obtained

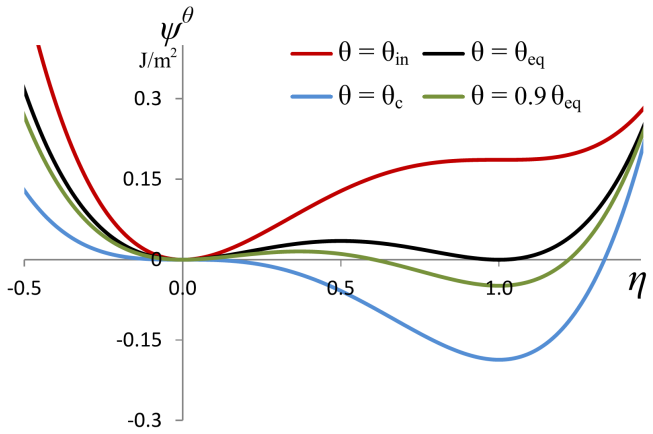

Figure 2.9 Thermal part of the thermodynamic potential ψ^θ vs. order parameter η for different temperatures. At equilibrium temperature θ_c , potential has two equal minima $\eta = 0$ and $\eta = 1$, corresponding to liquid and solid. For lower temperature (for example, $0.9\theta_e$), minimum corresponding to solid reduces (solid is thermodynamically stable), but there is an energy barrier between phases, i.e., liquid is metastable. At and below the melt instability temperature θ_c, the minimum corresponding to liquid disappears and melt is unstable. Similarly, at and above the solid instability temperature θ_i, the minimum corresponding to solid disappears and solid is unstable.

for macroscopic sample[1,3,8,15]: $H = 933.57 \times 10^6 J/m^3$, $K_m = 41.3GPa$, $K_s = 71.1GPa$, $\alpha_m = 4.268 \times 10^{-5}K^{-1}$, $\alpha_s = 3.032 \times 10^{-5}K^{-1}$, $\gamma_s = 1.050J/m^2$, $\Delta\gamma = 0.129J/m^2$, $\beta = 3.21 \times 10^{-10}N$, $\chi = 400m^2/Ns$, $\theta_c/\theta_e = 0.8$ (which leads to $\theta_i/\theta_e = 1.2$, $\theta_c = 746.9K$, and $\theta_i = 1120.40K$). To determine β we used $\gamma_{s-l} = 0.1J/m^2$ from[3] and Eq.(9), and to determine χ we used interface mobility $1.283m/(sK)$ obtained with MD simulation (Mendelev, M. private communication, 2010) and Eq.(11), both for plane interface. For such parameters, equilibrium interface thickness $\delta_e = 2.97nm$ (Eq.(9)).

Justification of the model of coherent interface and non-spherical transformation strain for melting

Below, we will show that in the framework of any phase-field theory, which takes into account finite interface width and elasticity, our model of coherent interface and non-spherical transformation strain for melting are straightforward and natural. First,

as in any phase-field theory, we assume continuity of displacements. Second, as in any phase-field theory, we assume that within interface any property varies from the value for solid to that of the melt; these should include shear modulus and transformation strain. Third, with this model and traditional assumption of pure volumetric transformation strain, we obtained large elastic stresses and energy inside the interface, which led to a large deviation of theory from experiments for thickness of the molten layer (Fig. 3) and size dependence of the melting temperature (Fig. 4). And fourth, it is clear that the missing physics is in the relaxation of elastic stresses, i.e., introducing an inelastic deviatoric strain (volumetric transformation strain is completely determined by the ratio of densities of phases). While it is completely unexpected and new for melting, the phase-field approach describes intermediate states between solid and melt, and the only reasons that transformation strain was accepted to be pure volumetric are the tradition and that the deviatoric part is unknown (in contrast to martensitic transformations). However, unknown does not mean that it is zero. It is clear that one has to develop a thermodynamically consistent kinetic equation for deviatoric part of the transformation strain, but this is a separate and complex problem. Thus, we considered the simplest limit case of uniaxial transformation strain normal to the interface, which minimizes internal stresses along the interface and their energy and does not require additional material parameters.

Since we obtained very reasonable (but not perfect) correspondence with experiments, we concluded in the paper that: the model of coherent solid-melt interface has good potential for the description of experiments; traditional volumetric ε_t is not adequate for large particles, i.e., there is interface restructuring, driven by the internal stress relaxation; and a thermodynamic and kinetic theory for ε_t should be developed.

Acknowledgements The support of National Science Foundation, Office of Naval Research, Air Force Office of Scientific Research, and Iowa State University are gratefully

acknowledged.

Author Contributions V.L. proposed the research and developed theory. K.S. performed the phase field simulations.

Author Information Correspondence should be addressed to V.L. (vlevitas@iastate.edu).

References

1. Denier van der Gon, A. W., Smith, R. J., Gay, J. M., OConnor, D. J. and van der Veen, J. F., Melting of Al surfaces. *Surf. Sci.* **227**, 143-149 (1990).

2. Henson, B. F. & Robinson J. M. Dependence of quasiliquid thickness on the liquid activity: A bulk thermodynamic theory of the interface. *Phys. Rev. Lett.* **92**, 246107 (2004).

3. Lai, S. L., Carlsson J. R. A. & Allen, L. H. Melting point depression of Al clusters generated during the early stages of film growth: Nanocalorimetry measurements. *Appl. Phys. Lett.* **72**, 1098-1100 (1998).

4. Levitas V. I., Pantoya M., Chauhan G. & Rivero I. Effect of the alumina shell on the melting temperature depression for nano-aluminum particles. *J. Phys. Chem. C* **113**, 14088-14096 (2009).

5. Puri, P. and Yang, V., Effect of particle size on melting of aluminum at nano scales. *J. Phys. Chem. C.* **111**, 11776-11783 (2007).

6. Ivanov, D. S. & Zhigilei, L. V. Combined atomistic-continuum modeling of short pulse laser melting and disintegration of metal films. *Phys. Rev. B*, **68**, 064114 (2003).

7. Iglev, H., Schmeisser, M., Simeonidis, K., Thaller, A. & Laubereau, A. Ultrafast superheating and melting of bulk ice. *Nature* **439**, 183-186 (2006).

8. Levitas, V. I., Asay, B. W., Son, S. F. & Pantoya, M. Mechanochemical mechanism for fast reaction of metastable intermolecular composites based on dispersion of liquid metal. *J. Appl. Phys.* **101**, 083524 (2007).

9. Grinfeld, M. A., *Thermodynamic Methods in the Theory of Heterogeneous Systems.* Sussex: Longman (1991).

10. Delogu, F. Mechanistic aspects of homogeneous and heterogeneous melting processes. *J. Phys. Chem. B* **110**, 12645-12652 (2006).

11. Lowengrub, J. & Truskinovsky, L. Quasi-incompressible Cahn-Hillard fluids and topological transitions. *Proc. R. Soc. London A* **454**, 2617-2654 (1998).

12. Anderson, D. M., McFadden, G. B. & Wheeler, A. A. A phase-field model of solidifcation with convection. *Physica D* **135** (2000).

13. Anderson, D. M., McFadden, G. B. & Wheeler, A. A. A phase-field model with convection: sharp-interface asymptotics. *Physica D* **151** (2001).

14. Slutsker, J., Thornton. K., Roytburd A. L., Warren, J. A. & McFadden, G. B. Phase field modeling of solidification under stress. *Phys. Rev. B* **74**, 014103 (2006).

15. Pluis, B., Frenkel, D. & Van der Veen, J. F. Surface-induced melting and freezing. 2. A semiempirical Landau-type model. *Surf. Sci.* **239**, 282-300 (1990).

16. Lipowsky, R., Critical surface phenomena at 1st-order bulk transitions. *Phys. Rev. Lett.* **49**, 1575-1578 (1982).

17. Chang, J. & Johnson, E. Surface and bulk melting of small metal clusters. *Philos. Mag.* **85**, 3617-3627 (2005).

18. Levitas, V. I., Levin, V. A., Zingerman, K. M. & Freiman, E. I. Displacive phase transition at large strains: Phase field theory and simulations. *Phys. Rev. Lett.* **103**, 025702 (2009).

19. Levitas, V. I. & Javanbakht, M. Surface tension and energy in multivariant martensitic transformations: Phase-field theory, simulations, and model of coherent interface. *Phys. Rev. Lett.* **105**, 165701 (2010).

20. Levitas, V. I., Preston, D. L. & Lee, D. W. Three-dimensional Landau theory for multivariant stress-induced martensitic phase transformations. *Phys. Rev. B* **68**, 134201 (2003).

21. Hoyt, J. J. Effect of stress on melting and freezing in nanopores. *Phys. Rev. Lett.* **96**, 045702 (2006).

22. Levitas, V. I., Lee, D. W. and Preston, D. L. Interface propagation and microstructure evolution in phase field models. Int. J. Plast., 26(3), 395-422, 2010. *Int. J. Plast.* **26**, 395-422 (2010).

CHAPTER 3. COHERENT INTERFACE WITH STRESS RELAXATION IN PHASE-FIELD APPROACH FOR MELTING / SOLIDIFICATION

Modified from a paper published in the Physical Review B, Rapid Communications

Valery I. Levitas[1] and Kamran Samani[2]

[1] *Iowa State University, Departments of Aerospace Engineering, Mechanical Engineering, and Material Science and Engineering, Ames, Iowa 50011, U.S.A.*

[2] *Iowa State University, Department of Mechanical Engineering, Ames, Iowa 50011, U.S.A.*

Abstract

An advanced Ginzburg-Landau (GL) approach to melting-solidification coupled with mechanics is developed. It is based on the concept of coherent solid-liquid interface with transformation strain tensor, the deviatoric part of which is described by a thermodynamically consistent kinetic equation. Due to relaxation of elastic energy, a promoting contribution to the driving force for phase transformation in the GL equation appears, both for melting and solidification. Good agreement with known experiments is obtained for Al nanoparticles for the size-dependent melting temperature and temperature-dependent thickness of the surface molten layer. All types of interface stress distributions from known molecular dynamic (MD) simulations are obtained and interpreted. A similar approach can be applied for sublimation-condensation, amorphization-vitrification, diffusive transformations and chemical reactions.

Introduction

Stresses within the few-nanometer-thick interface become currently a separate topic of interest in the thermodynamic and MD approaches[1] to melting because they affect significantly the thermodynamics and kinetics of melting. However, they were not studied in the phase-field or GL approaches. While the GL approach is widely used for modeling of pre-melting[2] and melting[3], mechanical issues have been addressed only recently for pre-melting[4] and melting[5, 4]. Thus, models for coherent solid-melt interface without[5] and with[4] surface tension were developed. However, the outstanding problem is related to the transformation strain tensor $\boldsymbol{\varepsilon}_t$ that transforms in unloaded state the elemental volume of one phase into another. For martensitic phase transformations, $\boldsymbol{\varepsilon}_t = 1/3\varepsilon_{0t}\boldsymbol{I} + \boldsymbol{e}_t$ transforms the crystal lattice of austenite into a lattice of martensite–i.e., the entire tensor is completely determined when lattices are known. Here, ε_{0t} is the volumetric transformation strain, $\boldsymbol{I}$ is the unit tensor, and $\boldsymbol{e}_t$ is the deviatoric transformation strain that characterizes change in shape. For melting and solidification, change in specific volume (or density) is known only, and it was always assumed the pure volumetric transformation strain $\boldsymbol{\varepsilon}_t = 1/3\varepsilon_{0t}\boldsymbol{I}$ and $\boldsymbol{e}_t = 0$. Such an assumption works well for sharp interface approaches[6]. However, for coherent, finite-width interface in the GL approach, pure volumetric transformation strain generates huge internal elastic stresses, which yields multiple contradictions with available experimental and MD results (see Figs. 1-4 below and[4]). Thus, the melting temperature for Al nanoparticle for radii $R > 20$ nm is getting larger than the bulk equilibrium melting temperature θ_e (Fig. 1). The relationship for the thickness of surface molten layer h vs. temperature θ for $R > 40$ nm is qualitatively different from experiments (Fig. 2). The interface stresses are an order of magnitude larger than in MD simulations[1] and may have an opposite sign (Fig. 3b). And finally, internal stresses lead to overestimation of the interface velocity (Fig. 4). These contradictions show the necessity of introducing and defining the deviatoric transformation strain $\boldsymbol{e}_t$, which will lead to stress relaxation. The fact

that it is unknown from geometric consideration does not mean it should be zero. Atoms during transformations can move in the way that reduces elastic energy and increases the driving force for transformation; this results in some deviatoric transformation strain in continuum description. In the paper, we expanded the phase-field theory for melting by developing the thermodynamically consistent kinetic equations for $\boldsymbol{e}_t$. This also results in additional contribution to the driving force for melting in the GL equation. The theory is applied for resolving all of the above contradictions in melting and pre-melting of Al nano- and large-size particles. Results are in good agreement with experiments for melting temperature vs. R and thickness of molten layer vs. θ, as well reproducing all types of distributions of interface stresses obtained with MD.

We designate contractions of tensors $\boldsymbol{A}$ and $\boldsymbol{B}$ over one and two indices as $\boldsymbol{A}\cdot\boldsymbol{B}$ and $\boldsymbol{A}\!:\!\boldsymbol{B}$, respectively; $\otimes$ designates a dyadic product, and $\overset{\circ}{\boldsymbol{\nabla}}$ and $\boldsymbol{\nabla}$ are the gradients in the undeformed and deformed states. The subscripts or superscripts e, t, and θ are for elastic, transformational, and thermal contributions to energy, strain, and stress; subscripts st and $*$ are for the surface tension and symmetrization, and $\Delta A = A_s - A_m$ is for any property A, with subscripts s and m for solid and melt.

Model

We will further develop our model with coherent solid-melt interface from[4]. For simplicity, viscosity is neglected and shear strain is small. Melting is described with the help of the order parameter η that varies from 1 in solid to 0 in melt. We will use decomposition of strain $\boldsymbol{\varepsilon} = 1/3\varepsilon_0\boldsymbol{I} + \boldsymbol{e}$ and stress $\boldsymbol{\sigma} = p\boldsymbol{I} + \boldsymbol{S}$ tensors into spherical and deviatoric parts with $p = \boldsymbol{\sigma}\!:\!\boldsymbol{I}/3$ for mean stress and ε_0 for volumetric strain. The standard relationship for strain $\boldsymbol{\varepsilon} = (\overset{\circ}{\boldsymbol{\nabla}}\boldsymbol{u})_*$ in terms of displacements $\boldsymbol{u}$ and equilibrium equations $\boldsymbol{\nabla}\cdot\boldsymbol{\sigma} = 0$ is used. The distinguished point in kinematic decomposition

$$\boldsymbol{\varepsilon} = \boldsymbol{\varepsilon}_e + \boldsymbol{\varepsilon}_t + \boldsymbol{\varepsilon}_\theta, \quad \boldsymbol{\varepsilon}_t = 1/3\,\varepsilon_{0t}(1-\phi(\eta))\boldsymbol{I} + \boldsymbol{e}_t; \tag{1}$$

with $\boldsymbol{\varepsilon}_\theta = (\alpha_m + \Delta\alpha\phi(\eta))(\theta - \theta_e))\boldsymbol{I}$ and $\phi(\eta) = \eta^2(3-2\eta)$ is the introduction of the deviatoric transformation strain $\boldsymbol{e}_t$ for melting, which is defined by a thermodynamically consistent kinetic equation (derived below)

$$\dot{\boldsymbol{e}}_t \;=\; 6\Lambda\eta(1-\eta)\boldsymbol{S}_e|\varepsilon_{0t}||\dot{\eta}|, \tag{2}$$

where α is the linear thermal expansion coefficient and $\Lambda \geq 0$ is the kinetic coefficient. The Helmholtz free energy per unit undeformed volume of solid ψ and its contributions are:

$$\begin{aligned}
\psi &= \psi^e(\varepsilon_0, \boldsymbol{e}, \eta, \theta) + J\breve{\psi}^\theta + \psi^\theta + J\psi^\nabla;\\
J &= \rho_0/\rho = 1 + \varepsilon_0;\\
\psi^e &= 0.5(K_m + \Delta K\phi(\eta))\varepsilon_{0\mathrm{e}}^2 + \mu\phi(\eta)\boldsymbol{e}_e{:}\boldsymbol{e}_e;\\
\psi^\theta &= H(\theta/\theta_e - 1)\phi(\eta); \quad \breve{\psi}^\theta = A\eta^2(1-\eta)^2;\\
\psi^\nabla &= 0.5\beta|\boldsymbol{\nabla}\eta|^2; \quad A := 3H(1-\theta_c/\theta_e).
\end{aligned} \tag{3}$$

Here, ρ_0 and ρ are the mass densities in the nondeformed and deformed states, K and μ are the bulk and shear modulus, β is the gradient energy coefficient, H is the heat of fusion, $\breve{\psi}^\theta$ is the double-well energy, and θ_c is the melt instability temperature. Despite the small strain approximation, one cannot simplify $J \simeq 1$ and $\boldsymbol{\nabla} \simeq \overset{\circ}{\boldsymbol{\nabla}}$, because in this case surface tension disappears. For such an energy, expressions for stress and the GL equation are:

$$\boldsymbol{\sigma} = \frac{\partial\psi}{\partial\boldsymbol{\varepsilon}} - J^{-1}\boldsymbol{\nabla}\eta\otimes\frac{\partial\psi}{\partial\boldsymbol{\nabla}\eta} = \boldsymbol{\sigma}_e + \boldsymbol{\sigma}_{st}; \tag{4}$$

$$\boldsymbol{\sigma}_e = (K_m + \Delta K\phi(\eta))\varepsilon_{0e}\boldsymbol{I} + 2\mu\phi(\eta)\boldsymbol{e}_e;$$

$$\boldsymbol{\sigma}_{st} = (\psi^\nabla + \breve{\psi}_\theta)\boldsymbol{I} - \beta\boldsymbol{\nabla}\eta\otimes\boldsymbol{\nabla}\eta; \tag{5}$$

$$\begin{aligned}
\frac{1}{\chi}\dot{\eta} = X_\eta = -J^{-1}\frac{\partial\psi}{\partial\eta}|_{\boldsymbol{\varepsilon}} + \boldsymbol{\nabla}\cdot\left(J^{-1}\frac{\partial\psi}{\partial\boldsymbol{\nabla}\eta}\right) = \beta\nabla^2\eta - \\
6J^{-1}[H\,(\theta/\theta_e - 1) + p_e\varepsilon_{0t} - \Lambda|\varepsilon_{0t}|\boldsymbol{S}_e{:}\boldsymbol{S}_e sign(\dot{\eta}) - \\
3p_e\Delta\alpha(\theta-\theta_e) + 0.5\Delta K\varepsilon_{0e}^2 + \mu\boldsymbol{e}_e{:}\boldsymbol{e}_e]\eta(1-\eta) - \\
4A\eta(1-\eta)(0.5-\eta),
\end{aligned} \tag{6}$$

where χ is the coefficient and X_η is the driving force for changing in η, determined from the expression for the dissipation rate $D = X_\eta \dot{\eta} \geq 0$. Because of the introduction of deviatoric transformation strain in Eq.(2), an additional promoting (for both melting and solidification) contribution to X_η, $6J^{-1}\Lambda|\varepsilon_{0t}|\boldsymbol{S}_e\boldsymbol{:}\boldsymbol{S}_e sign(\dot{\eta})$, appears. Because of this term, even stationary solution of Eq.(6) for η depends on Λ; due to Eq.(2), it depends on the entire evolution of $\boldsymbol{S}_e$ and $\boldsymbol{e}_t$ toward their stationary solutions. The coupled Eqs.(1)-(6) are solved for all problems below using the FEM code COMSOL.

To outline derivation of Eq.(2) and its contribution to the GL Eq.(6), we can neglect surface stresses and dependence of ψ on $\boldsymbol{\nabla}\eta$, and put $J \simeq 1$ for brevity; the final results are the same. Substituting ψ and Eq.(1) in the expression for the dissipation rate $D = \boldsymbol{\sigma}_e : \dot{\boldsymbol{\varepsilon}} - \dot{\psi} \geq 0$, and using independence of D of $\dot{\boldsymbol{\varepsilon}}_e$ and $\dot{\theta}$, one obtains Eq.(4) and $D = (p_e\varepsilon_{0t}\phi'(\eta) - \frac{\partial \psi}{\partial \eta})\dot{\eta} + \boldsymbol{S}_e : \dot{\boldsymbol{e}}_t \geq 0$. To allow change in $\boldsymbol{e}_t$ during transformation only, we put $\dot{\boldsymbol{e}}_t = 0$ for $\dot{\eta} = 0$. We also would like to impose that equation for $\dot{\boldsymbol{e}}_t$ is the same for both direct and reverse transformations. Then, in general, $\dot{\boldsymbol{e}}_t = f(\boldsymbol{S}_e, \eta, |\dot{\eta}|)$. Inequality $D \geq 0$ should be satisfied for all possible processes. Choosing p_e that satisfies $p_e\varepsilon_{0t}\phi'(\eta) = \frac{\partial \psi}{\partial \eta}$ at least for one time instant, one obtains $\boldsymbol{S}_e : \dot{\boldsymbol{e}}_t \geq 0$. Equation $\dot{\boldsymbol{e}}_t = \Lambda|\varepsilon_{0t}\dot{\phi}(\eta)|\boldsymbol{S}_e$ with $\Lambda \geq 0$ is the simplest one that satisfies all the above conditions and also scales $\dot{\boldsymbol{e}}_t$ with the rate of volumetric transformation strain. It coincides with Eq.(2). Since $|\dot{\eta}| = \dot{\eta}\, sign(\dot{\eta})$, substitution of Eq.(2) in D results in $\boldsymbol{S}_e$ related term $6\Lambda|\varepsilon_{0t}|\boldsymbol{S}_e : \boldsymbol{S}_e\eta(1-\eta)sign(\dot{\eta})\dot{\eta}$, which justifies that X_η should have the contribution shown in Eq.(6). During transformation, the evolution of $\boldsymbol{e}_t$ relaxes elastic deviatoric stress $\boldsymbol{S}_e$ and elastic energy, and this relaxation produces promoting contribution to X_η for both melting and solidification. Note that Eq.(2) leads to the maximization of the magnitude of the driving force X_η, which is in line with the postulate of realizability[7]. The thermodynamic procedure[11] that led to GL equation, also results in the boundary conditions[4]:

$$\begin{aligned} J\frac{\partial \psi}{\partial \boldsymbol{\nabla}\eta}\cdot\boldsymbol{n} &= \beta\nabla\eta\cdot\boldsymbol{n} = -\frac{d\gamma}{d\eta}, \\ \gamma(\eta) &= \gamma_l + (\gamma_s - \gamma_l)\phi(\eta), \end{aligned}$$

$$\sigma_n \;=\; -\frac{2\gamma(\eta)}{R} - \bar{p}, \tag{7}$$

where $\boldsymbol{n}$ is the unit normal to the boundary; $\gamma(\eta)$ is the specific surface energy with γ_l and γ_s for the surface energy of liquid and solid, respectively; σ_n is the normal to interface stress; $1/R$ is the mean curvature, and $\bar{p}$ is the external pressure. External pressure in all cases is considered to be zero. If surface energy does not change during melting, then $\gamma = const$ and Eq.(7) reduces to traditional boundary condition $\nabla\eta\cdot\boldsymbol{n} = 0$. As initial conditions, values of η and $\boldsymbol{e}_t$ in the entire volume are 0.99 and 0, respectively. For the interface velocity and its dependence on heating rate in Fig. 3, homogeneous temperature is prescribed by equation $\theta = 890$ K + (heating rate) t, where t is time in seconds.

We use the following material parameters for Al obtained for macroscopic sample [4, 8, 9, 10]: $\theta_e = 933.67K$, $H = 933.57 \times 10^6$ J/m^3, $K_m = 41.3$ GPa, $K_s = 71.1$ GPa, $\mu = 27.3$ GPa, $\varepsilon_{0t} = 0.06$, $\alpha_m = 4.268 \times 10^{-5}$ K^{-1}, $\alpha_s = 3.032 \times 10^{-5}$ K^{-1}, $\gamma_s = 1.050$ J/m^2, $\gamma_l = 0.931$ J/m^2, $\beta = 3.21 \times 10^{-10}$ N (which results in solid-liquid interface energy $\gamma_{sl} = 0.1$ J/m^2), $\chi = 400$ m^2/Ns, $\theta_c/\theta_e = 0.8$ (which leads to $\theta_i/\theta_e = 1.2$, $\theta_c = 746.9$ K, and the solid instability temperature $\theta_i = 1120.4$ K). For particles of radius R, homogeneously increasing temperature is prescribed, and stationary solutions have been determined for each temperature. Interface position corresponds to the point with $\eta = 0.5$. The thickness h of pre-molten and completely liquid surface layer was determined and plotted as a function of $\theta_e - \theta$ (Fig. 2). Melting temperature, θ_m, is defined as the temperature at which the stationary, two-phase solution loses its stability and the interface propagates to the center.

Results

In Fig. 1a, melting temperatures for models without ($\Lambda = 0$) and with ($\Lambda = 4\times10^{-2}$) deviatoric transformation strain are compared with experimental results; here and below

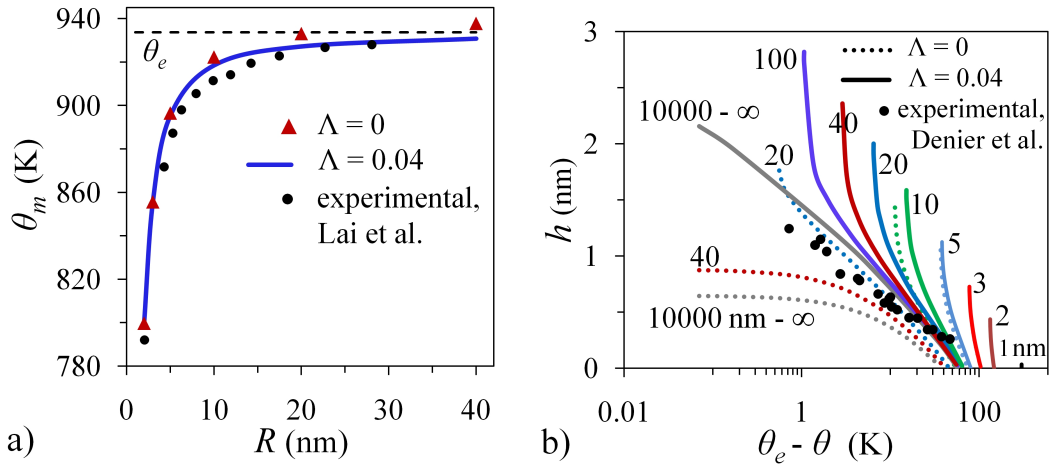

Figure 3.1 (a) Size dependence of melting temperature for Al nanoparticles for two different values of Λ (in MPa^{-1}) vs. experimental data[9] (dots). (b) Temperature dependence of the thickness of the molten surface for Al for different particle radii (shown in nm near curves) and values of Λ vs. experimental data[8] (dots).

Λ is in MPa^{-1}. This value of Λ represents the smallest one, above which θ_m does not practically reduce and $\theta_m = \theta_e$ for $R \to \infty$. For particles with $R < 10$ nm, surprisingly, both models yield equal melting temperature. For larger particles, neglecting deviatoric transformation strain introduces large internal elastic stresses that suppress melting, and consequently, melting temperatures are larger. For $R > 20$ nm and $\Lambda = 0$, melting temperature becomes larger than θ_e, which is contradictory and shows that such a model cannot be used. The model with deviatoric strain corresponds well to experiments. Note that internal stresses for $\Lambda = 0$ are mostly due to the tangential component $\varepsilon_{t\phi} = \varepsilon_{0t}/3 = 0.02$ of volumetric transformation strain, because radial expansion ε_{tr} at the interface does not experience resistance of solid. That is why in[4] radial transformation strain was assumed as the limit case. Here, we obtained that for relatively large particles with $R > 10$ μm, maximum $\varepsilon_{t\phi} = 0.018$–i.e., almost the entire total tangential strain relaxes. At the same time, for particles with $R = 5$ and 3 nm, which are under essential pressure due to surface tension, maximum $\varepsilon_{t\phi} = 0.0065$ and 0.001 only, respectively. That is why internal stress relaxation is not essential and does not affect θ_m.

In Fig. 1b, thickness h of the surface molten layer is plotted vs. $\theta_e - \theta$. For $R \leq 5$ nm, results based on models with and without stress relaxation are very close. For $R \simeq 20$ nm, the difference in h is large. For $R \geq 40$ nm, the curves differ qualitatively. While for the plane interface the results from the model with deviatoric strain are in good agreement with experimental data, results for $\Lambda = 0$ even show saturation (rather than divergence) in h and differ qualitatively from experiments.

In Fig. 2, distribution of radial σ_r and tangential σ_ϕ stresses with different values of Λ are shown. The dot in Fig. 2a is for the pressure in solid calculated with the Laplace equation $p_l - 2\gamma_{sl}/r_i$, which corresponds to the lack of elastic stresses (like for liquid-liquid interface). Such pressure can be achieved for $\Lambda = 3$, and it does not change at further increase in Λ. This value is two orders of magnitude larger than that required for independence of θ_m of Λ–i.e., comparison of stress distribution with experiment or MD results is a much more sensitive method to determine Λ than comparison of θ_m. The reason for deviation from Laplace equation is the elastic tangential stresses. At smaller values of Λ, the pressure jump reduces, then changes sign, and for $\Lambda = 0$ it even leads to tensile pressure in the solid core. At the same time, a realistic curve is between the curves for $\Lambda = 3 \times 10^{-2}$ (above which θ_m is independent of Λ) and $\Lambda = 3$–i.e., results without deviatoric transformation strain are completely inadequate.

In Fig. 2b, distributions of tangential stress σ_ϕ and its elastic σ_e and surface tension σ_{st} contributions across the plane solid-melt interface are shown. For $\Lambda \geq 4$, σ_e completely relax, and the total stress coincides with the surface tension $\sigma_{st} > 0$. Since volumetric transformational expansion generates compressive elastic tangential stresses σ_e, total tangential stress may be completely tensile, or compressive, or may vary from compressive to tensile stress while moving from solid to melt, depending on the degree of relaxation of elastic stresses. Plots of total tangential stresses in Fig. 2b reproduce typical stress distributions and proper magnitude of plots for different crystal faces in MD simulations[1] and allow one to explain the reasons for such a variety and nontrivial shape

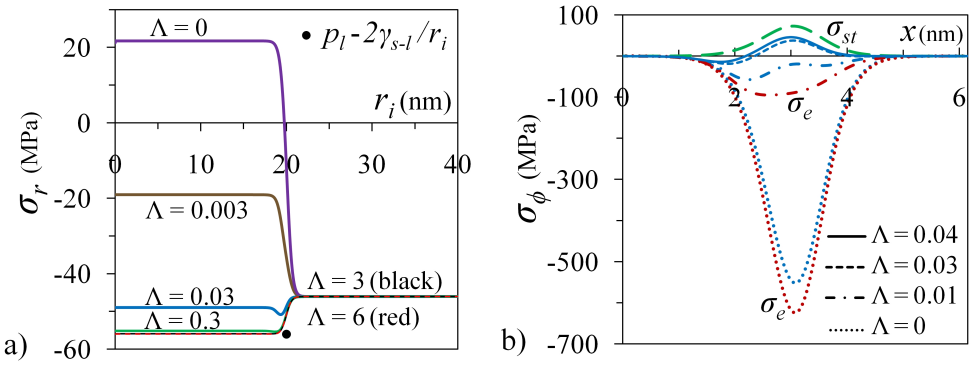

Figure 3.2 (a) Distributions of radial stresses in Al particle with $R = 40$ nm for interface position $r_i = 20$ nm at $\theta = \theta_e$ for different values of Λ. Dot corresponds to the pressure in solid calculated with the Laplace equation $p_l - 2\gamma_{sl}/r_i$. (b) Distributions of tangential stress σ_ϕ and its elastic σ_e and surface tension σ_{st} contributions across the plane solid-melt interface at $\theta = \theta_e$. Surface tension σ_{st} (Eq. (5)) is the same for all cases. Four unmarked curves are for total stresses.

of distributions. Note that the elastic stresses only contribute to GL Eq.(6); surface tension affects melting by changing the distribution of elastic stresses. For $\Lambda = 0$, the magnitude of compressive stresses is much larger than in MD simulations[1]; this causes an unrealistic increase in melting temperature above θ_e. The model of coherent solid-melt interface with proper surface tension was introduced in[4], but only after introduction of stress relaxation and the ability to reproduce and explain typical stress distributions in MD simulations[1], can one claim the conceptual validity of this model.

Melting under a high heating rate and overheating are not only of fundamental interest, but have also applied significance–e.g., for the melt-dispersion mechanism of reaction of Al nanoparticles[10]. Interface velocities v are shown in Fig. 3 for two heating rates, 10^{12} K/s and 10^{13} K/s. Due to small particle size, homogeneous temperature is justified [10]. For 10^{13} K/s, interface propagation stops at $r_i = 25.9$ nm because homogeneous melt nucleation and reduction of η in the region $r_i < 25.9$ nm completes melting faster. An increase in Λ decreases interface velocity, and the difference with the case with $\Lambda = 0$ is larger for higher heating rate and smaller interface radii. Dots in Fig. 3 correspond to

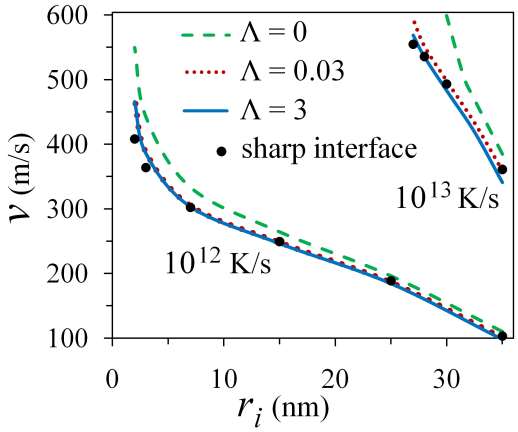

Figure 3.3 Interface velocity vs. interface position for different heating rates and $\Lambda = 0$. Dots corresponds to analytical solution[4]. The two lowest curves for different Λ coincide.

the analytical solution[4].

Our results for $\Lambda = 3 \times 10^{-2}$ and 3 are close to each other and to the sharp-interface solution, while for $\Lambda = 0$ interface velocity is significantly higher. The promoting effect of the elastic stresses on interface propagation (which confronts their suppressive effect on initiation of melting) is consistent with the analytical solution[4], i.e. to the linear relationship between v and the thermodynamic force for interface propagation per unit deformed volume of solid X when internal stresses are neglected:

$$\begin{aligned} v &= 6X\chi\sqrt{\beta\rho_m/(2A\rho_s)}, \\ X &= \frac{\rho_s}{\rho_{0s}}H\left(1-\frac{\theta}{\theta_e}\right)+p_m\left(\frac{\rho_s}{\rho_m}-1\right)-\frac{1}{2}\left(\frac{p_m^2}{K_m}-\frac{p_s^2}{K_s}\right)+\frac{2\gamma_{s-l}}{r_i}. \end{aligned} \qquad (8)$$

The elastic energy effectively increases γ_{s-l} and, consequently, the driving force. Note that the temperature at some points in Fig. 3 significantly (up to 200 K) exceeds the instability temperature of solid θ_i; still the sharp interface approach gives good results.

In Fig. 4, tangential deviatoric transformation strain and elastic stress are shown for $R = 40$ nm and different interface positions at $\theta = 930.8$ K. For all interfaces, there is the common curve characterizing residual deviatoric strain at each point after interface

passes through, and the major part of curves for each specific interface position is above it. This results in compressive elastic deviatoric stresses with the maximum below 10 MPa. However, when the curve for an individual interface in Fig. 4a falls below the common curve, tensile deviatoric stresses appear in Fig. 4b. With decreasing r_i, smaller deviatoric strain is required to reduce elastic stresses to the same and even a lower level.

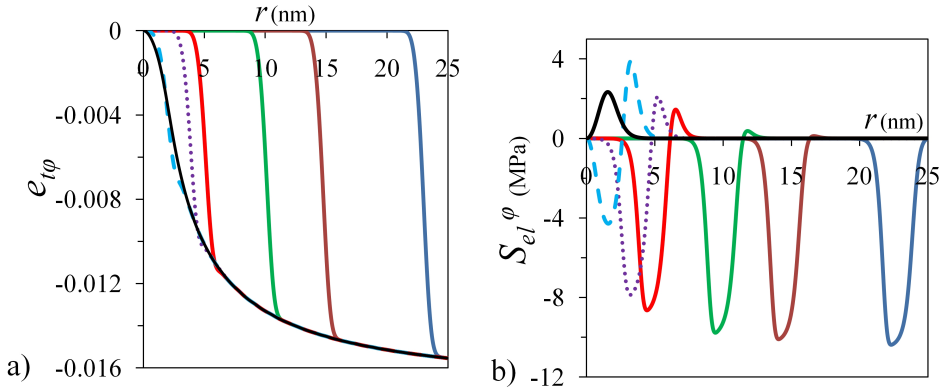

Figure 3.4 Tangential deviatoric transformation strain (a) and elastic stress (b) for $R = 40$ nm and $\Lambda = 0.04$, and $\theta = 930.8$ K at different interface positions.

In summary, an advanced GL model for the coherent solid-melt interface with transformation strain tensor, the deviatoric part of which is described by a thermodynamically consistent kinetic equation, is developed. Corresponding relaxation of elastic energy produces a promoting contribution to the driving force for phase transformation in the GL equation, both for melting and solidification. All types of interface stress distributions from known MD simulations are obtained as a combination of surface tension and elastic stresses with different degrees of relaxation. Without deviatoric transformation strain, elastic stresses are overestimated by a factor of 5 to 10, which leads to qualitative contradictions in the size dependence of melting temperature and temperature dependence of the thickness of the surface molten layer. With the kinetic equation for $\boldsymbol{e}_t$, good agreement for both these relationships with experiments for Al nano- and large-size particles is obtained. Results can be generalized for large strain using methods developed in[11]. A similar approach can be applied for sublimation-condensation[12], amorphization-

vitrification[12], chemical reactions[7], and other transformations for which $\boldsymbol{e}_t$ is not determined by geometry, both with and without the phase-field approach.

Support of NSF, AFOSR, and ARO is acknowledged.

References

1. T. Frolov and Y. Mishin, Modelling Simul. Mater. Sci. Eng. **18**, 074003 (2010); T. Frolov and Y. Mishin, Physical Review B **82**, 174114, (2010).

2. R. Lipowsky, Phys. Rev. Lett. **49**, 1575 (1982); J. Chang and E. Johnson, Philos. Mag. **85**, 3617 (2005).

3. D. M. Anderson, G. B. McFadden and A. A. Wheeler, Physica D **135**, 175 (2000); J. Lowengrub and L. Truskinovsky, Proc. R. Soc. London A **454**, 2617 (1998).

4. V. I. Levitas and K. Samani, Nature Comm. **2**, 284 (2011).

5. J. Slutsker, K. Thornton, A. L. Roytburd, J. A. Warren and G. B. McFadden, Phys. Rev. B **74**, 014103 (2006).

6. M. A. Grinfeld, *Thermodynamic Methods in the Theory of Heterogeneous Systems* (Sussex: Longman, 1991); M. A. Grinfeld, Doklagy Akad. Nauk SSSR, **251**, 10 (1980).

7. V. I. Levitas, V. F. Nesterenko and M. A. Meyers, Acta Materialia, **46**, 5929 (1998); V. I. Levitas, Int. J. Plasticity, **16**, 805 (2000).

8. A. W. Denier van der Gon, R. J. Smith, J. M. Gay, D. OConnor and J. van der Veen, Surf. Sci. **227**, 143 (1990).

9. S. L. Lai, J. R. A. Carlsson and L. H. Allen, Appl. Phys. Lett. **72**, 1098 (1998).

10. V. I. Levitas, B. W. Asay, S. F. Son and M. Pantoya, J. Appl. Phys. **101**, 083524 (2007); V. I. Levitas, Combustion and Flame, **156**, 543 (2009).

11. V. I. Levitas and M. Javanbakht, Phys. Rev. Lett **105**, 165701 (2010); V. I. Levitas, V. Levin, K. Zingerman and E. Freiman, Phys. Rev. Lett. **103** 025702 (2009); V. I. Levitas and D. Preston, Phys. Lett. A **343**, 32 (2005).

12. V. I. Levitas and N. Altukhova, Phys. Rev. Lett. **101**, 145703 (2008); V. I. Levitas, Phys. Rev. Lett. **95**, 075701. (2005).

CHAPTER 4. MELTING/SOLIDIFICATION OF NANOPARTICLES: NEW SCAL EFFECTS, THERMALLY ACTIVATED SURFACE NUCLEATION AND BI-STABLE STATES

Paper to be submitted to the Nature Materials

Valery I. Levitas[1] and Kamran Samani[2]

[1] *Iowa State University, Departments of Aerospace Engineering, Mechanical Engineering, and Material Science and Engineering, Ames, Iowa 50011, U.S.A.*

[2] *Iowa State University, Department of Mechanical Engineering, Ames, Iowa 50011, U.S.A.*

Abstract

While study of surface melting/melting/solidification of nanoparticles is of great fundamental and applied importance and a lot of progress is achieved, many of effects and surprises are still to be predicted. Here we advanced the phase field approach to melting by introducing the finite width Δ_ξ of the external surface layer (particle-gas interface) as the new scale parameter, which leads to revealing various phenomena and previously unknown scale effects. Strong dependence of the melting temperature for nanoparticles of various radii and the width of the molten surface layer on Δ_ξ is found and comparison with experiments led to an estimate for Δ_ξ for Al in the range of 0.35 - 0.7 nm. In addition to traditional continuous barrierless surface melting for $\Delta_\xi = 0$, barrierless jump-like

surface melting and thermally activated surface melting via critical nucleus (CN) are revealed. Very rich temperature $\theta - \Delta_\xi$ transformation diagram is found, which includes various barrierless and thermally activated transformations between solid, melt, and surface melt, and complex hysteretic behavior under various temperature and Δ_ξ trajectories. Bi-stable states (i.e., thermally activated switching between two states) between solid and melt is found for 2 nm particle and between solid and surface melt for up to 5 nm particles, in a Δ_ξ-dependent temperature range. Obtained results open unexplored direction of controlling surface melting and melting/solidification by controlling width of the external surface and utilizing predicted phenomena. They also can be expended for other phase transformations (e.g., amorphization, diffusive and electromagnetic transformations) and phenomena.

Introduction

Melting/solidification of nanoparticles and surface-induced premelting and melting are fundamental problems with significant applied interest. Thus, melting / amorphization / recrystallization of nanostructures are the main processes in the phase changed materials utilized in memory devices[1] and energy-saving technologies[2]. Melting plays an important role in the combustion of nanoparticles[3]. Surface melting increases reactivity of substances (e.g., explosives[4]), leads to reshaping of nanoobjects[5], and to transformation from one solid phase to another[5], which otherwise cannot nucleate. Fundamental interest is related to understanding of behavior of materials with comparable bulk and surface energy; size-dependent melting at temperatures θ, when bulk melt is not only deeply in the region of stability of solids, but even unstable[6, 7, 8, 9, 10, 11, 12]; appearance of the few nm size premolten and molten surface layer much below bulk melting temperature θ_e[13, 14, 6, 7, 8, 9, 11, 12]; melting of the particles with size comparable to the size of solid-liquid interface and surface melt, which may be in the heterogeneous intermediate state between solid and melt[6, 7, 8, 9, 12]; and spontaneous multiple switching between

solid and melt in the few nm size particles leading to bi-stable state[9, 15]. While molecular dynamics (MD) can in principle handle some of the above problems[9, 16], phase field approach (PFA) is an ideal continuum tool to study all the above phenomena. It utilizes thermodynamic and kinetic parameters (determined by experiment and MD) and may be applicable at larger time and space scales than MD; in some cases (see[7] and here), it gives even better description of melting of nanoparticles than MD.

Despite the significant progress in PFA to melting of nanoparticles[7, 8, 12], there is one important drawback: while PFA resolves finite width interfaces and surface molten layer, external surface is considered as the sharp one, while it has comparable width. Recently [17], we developed phase field approach to martensitic transformations which resolves a finite width of the plane external surface and revealed multiple coupled effects of Δ_ξ and mechanics and morphological transitions in the surface layer. While these effects and transitions are not relevant for melting, here we will modify theory[17] for the description of melting of nanoparticles and applied it to predictions and comprehensive study of new scale effects. Note that Δ_ξ can be varied by changing external media and by surface treatment. It is found that this neglected parameter, Δ_ξ strongly affects the melting temperature for nanoparticle of any radius R and the width of the molten layer h. In fact, for small dimensionless $\bar{\Delta}_\xi = \Delta_\xi/\Delta_\eta$, where Δ_η is the equilibrium width of the solid-melt interface, melting temperature slightly reduces with increasing $\bar{\Delta}_\xi$. There is a critical $\bar{\Delta}^*_\xi$ (reducing with reduced particle radius R), above which system behavior drastically changes. Thus, barrierless melting temperature has jump in slope and grows significantly with increasing $\bar{\Delta}_\xi$. Such a drastic change is caused by the disappearance of barrierless surface melting, i.e., particle remains solid until it barrierlessly completely melts. However, for $\bar{\Delta}_\xi > \bar{\Delta}^*_\xi$, other stable solution for the surface molten layer appears, which cannot be reached barrierlessly, but can be achieved by thermal activation, provided that the kinetic nucleation criterion is met. Consequently, one more unstable solution for the surface melt is found, which represents a critical nucleus between solid

and molten surface layer. While at relatively high temperatures critical nucleus covers part of the surface, it unexpectedly transforms to the spherical shell with reduced temperature. One more regime of surface melting below $\bar{\Delta}_\xi^*$ and above $\bar{\Delta}_\xi^d$ represents a jump-like (discontinuous) appearance of the molten layer, which causes temperature hysteresis in transformations between solid and surface melt. At another, larger, critical value $\bar{\Delta}_\xi^c$, stable surface melt ceases to exists and surface critical nucleus leads directly to complete melting. Also, for small $\bar{\Delta}_\xi$ and even for sharp external surface, when barrierless melting through continuous or discontinuous surface melt is possible, thermally activated melting occurs slightly below barrierless melting temperature (e.g., by 5.4 K for Al nanoparticles with radius $R = 5$ nm), which should be taken into account in interpretations of experiments. All these and other results are summarized into quite sophisticated temperature-Δ_ξ transformation diagram for barrierless and thermally activated melting, which also includes barrierless and thermally activated solidification and transformation from melt to surface melt. While some of transformations are possible at fixed $\bar{\Delta}_\xi$ and variable temperature, other can occur at variable $\bar{\Delta}_\xi$ only. In particular, surface melting at large $\bar{\Delta}_\xi$ is achievable during the $\bar{\Delta}_\xi$ increase only, leading to complex processes for different $\theta - \bar{\Delta}_\xi$ trajectories. Finally, in one of the regions of $\theta - \bar{\Delta}_\xi$ transformation diagram, transitions in both directions can occur via thermal fluctuations. This leads to bi-stable states and switching between them. Thus, switching between solid and melt is found for 2 nm particle, which is in agreement with MD simulations [9] and experiments[15]. Bi-stable state between solid and surface melt is predicted for up to 5 nm particles. Obtained results introduce thermally activated nucleation in PFA for melting/surface melting/solidification of nanoparticles; change interpretation of experimental data, which is different for slow and very fast heating, and open unexplored direction of controlling surface melting and melting/solidification by controlling $\theta - \bar{\Delta}_\xi$ through changing surrounding medium and surface treatment.

Phase field model

In addition to the order parameter η for melting with the values of 0 and 1 for melt and solid, respectively, we introduce the order parameter ξ that describes transition between particle (solid or melt) and surrounding material (e.g., gas) at external surface layer, which is 0 for particle and 1 for surrounding. The Helmholtz free energy per unit volume can be written as:

$$\psi = \psi^{\theta} + \psi^{\nabla} + \psi^{\xi} \tag{1}$$

$$\psi^{\theta} = H(\theta/\theta_e - 1)\phi(\eta) + 3H(1 - \theta_c/\theta_e)\eta^2(1-\eta)^2\,; \quad \psi^{\nabla} = 0.5\beta|\nabla\eta|^2 \tag{2}$$

$$\phi(\eta) = \eta^2(3 - 2\eta) \tag{3}$$

where ψ^{θ} and ψ^{∇} are thermal energy and gradient energy, respectively, θ_c is the melt instability temperature, ∇ and β are the gradient operator and gradient energy coefficient, H is the heat of fusion, and ψ^{ξ} is energy of the external surface layer. Since we do not intend to study evaporation of particle, we assume the simplest expression for ψ^{ξ} for equilibrium evaporation temperature:

$$\psi^{\xi} = J\xi^2(1-\xi)^2 + 0.5\beta_{\xi}(\nabla\xi)^2 = \frac{\gamma(\eta)}{\Delta_{\xi}}(0.542\Delta_{\xi}^2(\nabla\xi)^2 + 16.62\xi^2(1-\xi)^2) \tag{4}$$

where J and β_{ξ} are the material parameters. They are expressed through the width of the surface layer Δ_{ξ} and the variable surface energy $\gamma(\eta)$ of the external surface (different for solid and melt) from the condition that stationary planar particle-gas interface $\xi_s(r)$ (see Eq.(7)) has energy $\gamma(\eta)$[17]. Width Δ_{ξ} is defined as the distance between points where $\phi(\xi_s(r)) = 0.01$ and 0.99. Using an irreversible thermodynamic procedure based on the application of the first and second laws of thermodynamics to the system with energy depending on the gradient of the order parameter, and assuming linear relation between thermodynamic force and flux, the following expressions for the Ginzburg-Landau (GL) equation for η and ξ can be obtained[17]:

$$\frac{1}{\chi}\frac{\partial\eta}{\partial t} = -\frac{\partial\psi}{\partial\eta} + \nabla.\left(\frac{\partial\psi}{\partial\nabla\eta}\right) \tag{5}$$

$$\frac{1}{\chi_\xi}\frac{\partial \xi}{\partial t} = \frac{\gamma(\eta)}{\Delta_\xi}(1.083\Delta_\xi^2\nabla^2\xi - 66.48\xi(1-\xi)(0.5-\xi)) + 1.084\Delta_\xi\nabla\gamma(\eta).\nabla\xi \quad (6)$$

where χ and $\chi_\xi >> \chi$ are the kinetic coefficients. We assume a quasi-stationary surface layer profile:

$$\xi_s = [1 + exp(5.54(R-r)/\Delta_\xi)]^{-1} \quad (7)$$

and neglect its slight variation with heterogeneous variation of η. This is equivalent to consideration of stationary solution to Eq.(6) with neglected last term. Strictly, Eq.(7) is an analytical solution for a planar interface; however we found numerically that it describes well profile for a spherical interface down to few nm particles. Only half of particle-surrounding interface with $0 \leq \xi_s \leq 0.5$ belongs to the particle r. Thus, we prescribed this part with double energy and applied boundary condition $d\eta/dr = 0$ at $r = R$. This is equivalent to the consideration of the entire surface layer, but more convenient for computations. Numerical approach is described in the Method section.

For aluminum nanoparticles, the following material properties are used[8]: $H = 933.57\times 10^6 J/m^3, \beta = 3.21 \times 10^{-10} N$ (which corresponds to equilibrium solid-melt interface energy $\gamma_{sl} = 0.1\, J/m^2$ and width $\Delta_\eta = 3\, nm$), $\theta_e = 933.67\, K, \theta_c = 746.9\, K, \chi = 400\, m^2/Ns$, $\gamma(\eta) = \gamma_s + (\gamma_s - \gamma_l)\phi(\eta)$ with $\gamma_s = 1.05\, J/m^2$ and $\gamma_l = 0.931\, J/m^2$ for solid and melt.

Results

Barrierless transformations

$\theta - \bar{\Delta}_\xi$ diagram obtained by temperature variation at fixed surface layer thicknesses

Fig.(4.1) shows transformation curves and regions of existence of different phases (nanostructures) obtained by increasing/decreasing temperature at different fixed surface layer thicknesses, $\bar{\Delta}_\xi$ obtained by solution of Eq.(5), i.e., without thermal fluctuations. At small $\bar{\Delta}_\xi$, solid black curve S↔SM designates continuous hysteresis-free two way

transformation between solid, S and surface molten layer, SM. Along this line, minimum value of η reaches ~ 0.95, which is considered as appearance of the surface melt. This value continuously decreases down to some critical value η_c with the temperature increase, and increases up to one with temperature decrease.

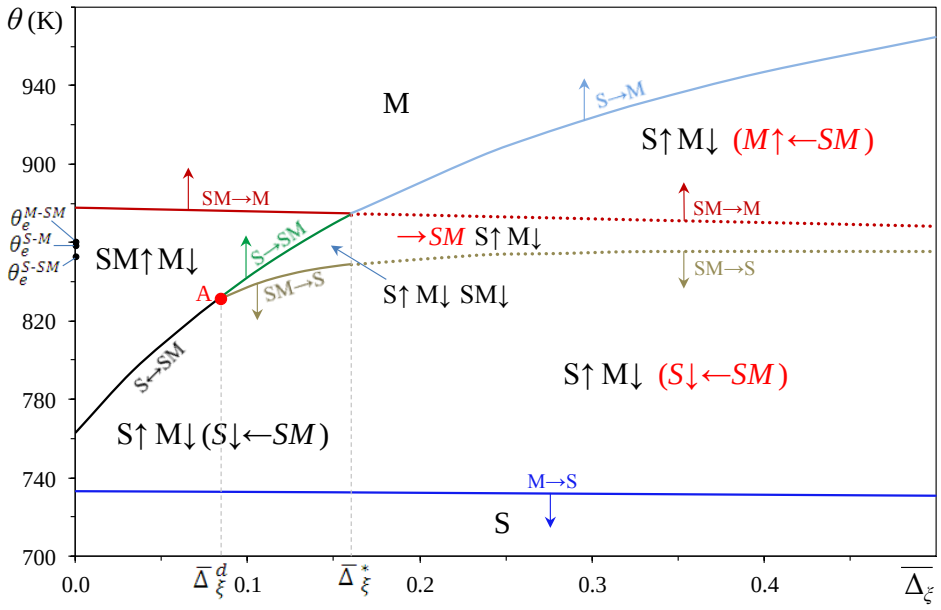

Figure 4.1 Temperature for barrierless transitions between different phases vs. dimensionless surface layer thickness $\bar{\Delta}_\xi$, for R = 5 nm.

When increasing temperature, the molten surface layer grows until it loses its stability (when $\eta = \eta_c$ at $r = R$) and transforms to homogeneous melt (M) along red curve SM→M, which is usually interpreted as melting temperature θ_m. Note that for semi-infinite sample (R→ ∞), $\eta_c = 0$ and transition to melt is smooth[7, 8]. Melting temperature for small $\bar{\Delta}_\xi$ slightly reduces with $\bar{\Delta}_\xi$: θ_m= 877.62 - 18.29$\bar{\Delta}_\xi$ and is well below the bulk melting temperature θ_e = 933.67 K. This is related to fact that the dimensionless thickness of the molten layer when it loses its stability is ~3.3 nm and much larger than $\bar{\Delta}_\xi$. After completely molten phase is obtained, reducing temperature does not yield phase transformation until dark blue curve M→S is reached, where melt transforms directly to solid missing surface molten layer. Solidification starts at the

center and propagates through particle. Note that solidification occurs below the melt instability temperature $\theta_c = 746.9$ K, i.e., when free energy even does not have minimum for bulk melt. Solidification temperature is $\theta_s = 733.3 - 5\bar{\Delta}_\xi$ and slightly reduces with $\bar{\Delta}_\xi$. Overcooling for barrierless solidification is also related to higher surface energy of solid than melt and small particle size. If temperature is reduced after molten layer is obtained but before reaching melting line SM→M, surface melt transforms to solid along black curve S↔SM for $\bar{\Delta}_\xi < \bar{\Delta}_\xi^d = 0.083$. Red dot, with $\bar{\Delta}_\xi = \bar{\Delta}_\xi^d$, and $\theta^d = 830.9$ K represents the point of appearance of jump-like transition from solid to molten layer, S→SM transformation. Thus, at this point, the minimal value of η jumps from 1 to 0.74 at surface, instead of a continuous reduction.

For larger $\bar{\Delta}_\xi$ values, solid transforms to molten layer along the green curve S→SM during heating, while with temperature reduction (before complete melting), reverse transition SM→S occurs along brown curve. Thus, the line S↔SM for continuous transformation splits into two lines for direct and reverse transformations with the hysteresis region between them. Again, if temperature is increased after surface melt is obtained, the surface melt transforms discontinuously to melt along the red line SM→M. So, in the triangular region between green S→SM and brown SM→S curves, designation S↑M↓SM↓ means that the particle is in solid state when temperature is increasing from the solid state S, in surface melt state when temperature is decreasing from surface melt state SM, and in molten state, when temperature is decreasing from the melt M. Below the black and brown curves, designation S↑ M↓ (S↓ ←SM) means particle is in the solid state when temperature is increasing from the solid state S; in the molten state, when temperature is decreasing from the melt M, and in solid state when temperature decreases from surface melt state SM.

After intersection of green S→SM and red SM→M curves at $\bar{\Delta}_\xi = \bar{\Delta}_\xi^* = 0.16$, solid transforms directly to melt along light blue curve S→M, without surface melting. Lack of the surface melting leads to drastic increase in the barrierless melting temperature

and jump in slope of the melting curve at $\bar{\Delta}_\xi = \bar{\Delta}_\xi^*$. Note that melting temperature and $\bar{\Delta}_\xi^*$ reduce with reduction in particle size, starting with $\theta_m = \theta_e$ and $\bar{\Delta}_\xi^* = 0.23$ for plane interface (Fig.4.2). For plane interface, melting temperature is constant below $\bar{\Delta}_\xi^*$. After melt is obtained, reducing temperature changes melt to solid along dark blue line M→S.

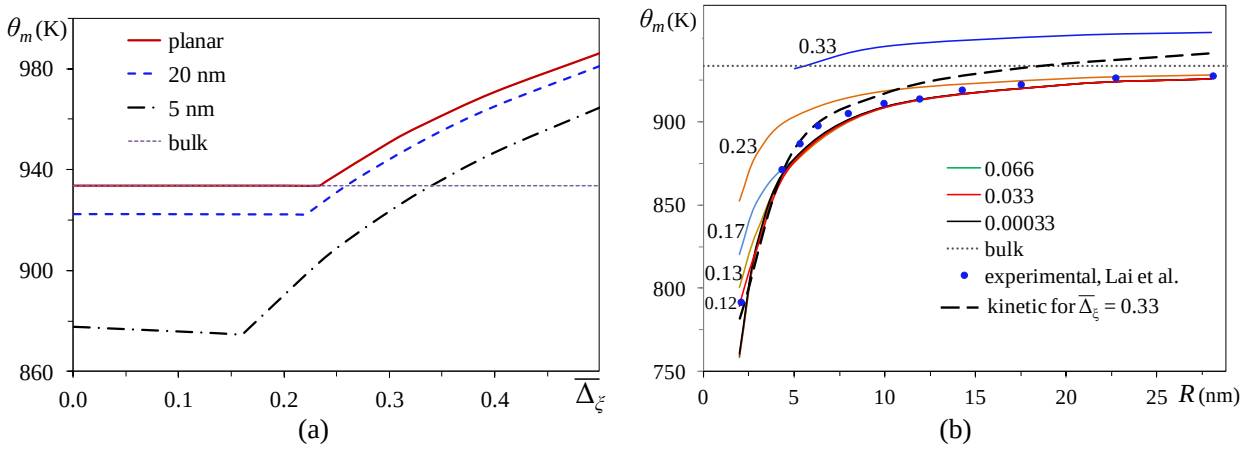

Figure 4.2 Barrierless melting temperature vs. $\bar{\Delta}_\xi^*$ for particles of different sizes (a) and vs particle size at different $\bar{\Delta}_\xi^*$ (b).

Transformation $\theta - \bar{\Delta}_\xi$ diagram at variable surface layer thicknesses and temperature

When variable surface layer thicknesses is allowable, two additional transformation curves should be included. Thus, if we start from the surface melt for $\bar{\Delta}_\xi < \bar{\Delta}_\xi^*$ and change $\bar{\Delta}_\xi^*$ and temperature within region between two dotted lines in Fig. 1, it will remain as a surface melt. If starting from the surface melt we change $\bar{\Delta}_\xi$ and temperature in a way that we cross the brown dotted line SM→S, a molten layer transforms to solid. If we cross the red dotted line SM→M, surface melt completely melts. Note that for $\bar{\Delta}_\xi > \bar{\Delta}_\xi^*$, if we started with solid or melt, nothing happens when we cross the dotted lines and a surface melting cannot be obtained. Also note that all solid lines keep their meaning when they are crossed by simultaneous change in surface layer thicknesses and temperature or any

of these parameters alone. Arrows ↑ or ↓ mean that the line is crossed from below or above, but not necessarily at constant $\bar{\Delta}_\xi$. Possibility of changing $\bar{\Delta}_\xi$ adds two more designations for the phase states in different regions, designated in red. Thus, above the dotted line SM→M, an additional region (M↑←SM)of melt obtained from a surface melt appears, and below the dotted line SM→S, an additional region (S↓←SM) of solid obtained from a surface melt is possible.

Barrierless melting temperatures vs particle size R for various $\bar{\Delta}_\xi$ values are shown in Fig.4.2.b along with experimental results from[6]. While for 5 nm $< R <$ 20 nm results for all $\bar{\Delta}_\xi < \bar{\Delta}_\xi^*$ are close to experiments, for $R = 2$ nm, the best fit to experiments is for $\bar{\Delta}_\xi = 0.117$. However, $\bar{\Delta}_\xi$ depends on surrounding medium and conditions at the surface.

Thermally activated transformations

While for $\bar{\Delta}_\xi > \bar{\Delta}_\xi^*$ there is no surface melt solution that can be obtained barrierlessly by increasing temperature, other stable solution for the surface molten layer appears, which can be obtained from initial conditions $\eta = 1$ for $r < r^*$ and $\eta = 0$ for $r^* \leqslant r \leqslant R$. Such solution can be achieved from solid by thermal activation, provided that the kinetic nucleation criterion is met. That also means that one more unstable stationary solution for the surface melt should be found, which represents a critical nucleus between solid and molten surface layer. Thus, solutions for the critical nuclei have been found (see Methods) for various $\theta, \bar{\Delta}_\xi$ and R and its energy is evaluated. For 5 nm particle and $\bar{\Delta}_\xi = 0.17$ (Fig. 3), a non-spherical critical nucleus between solid and molten layer changes to a spherical one as temperature reduces, which is quite unexpected geometry. The spherical critical nucleus can be obtained using a 1-D model, which reduces computational time by at least two orders of magnitude. Melting temperatures obtained using the 1-D model are within 2 K difference of those obtained from the non-spherical model, which is within acceptable difference range. It is interesting that the profile does not follow a monotonic

trend with temperature, as shown in Fig. 4.3.c.

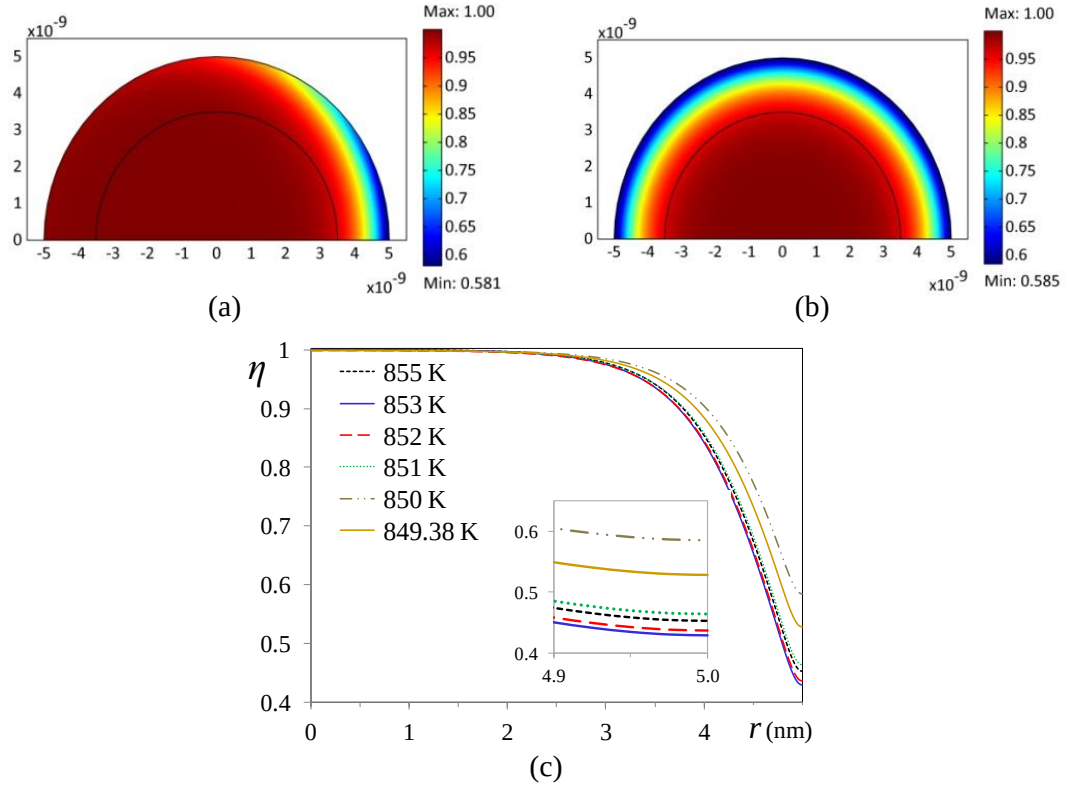

Figure 4.3 Critical nucleus at 860 K (a) and 850 K (b) and in the temperature range (c) for 5 nm particle with $\bar{\Delta}_\xi = 0.17$.

We accept traditional criterion for thermally activated nucleation, $\Delta \mathrm{E} = E_{CN} - E \leqslant 40k\theta$, where E_{CN} and E are the energies of the critical nucleus and a specific state from which it jumps to the critical nucleus, respectively, and k is the Boltzmann′s constant. In Fig. 4.4.a, below 856.2 K, the difference between energies of critical nucleus and surface melt is below $40k\theta$, i.e., system can jump from surface melt to critical nucleus. After solution for the critical nucleus is introduced as an initial condition, small positive perturbations in η lead to stationary solid, while small negative perturbations return it back to surface melt. At 849.38 K, energies of a critical nucleus and surface melt are equal (Fig. 4). At 849.37 K, molten layer transforms barrierlessly to solid and critical nucleus

ceases to exist. Above 849.38 K, a jump from solid to CN is possible as well, leading to appearance of molten layer, which exists up to 873.25 K. An important conclusion is that in the range 849.38 K and 856.2 K both direct and reverse transformations between solid and surface melt are kinetically possible. That means that system will switch spontaneously in time between these two states, exhibiting bi-stable state.

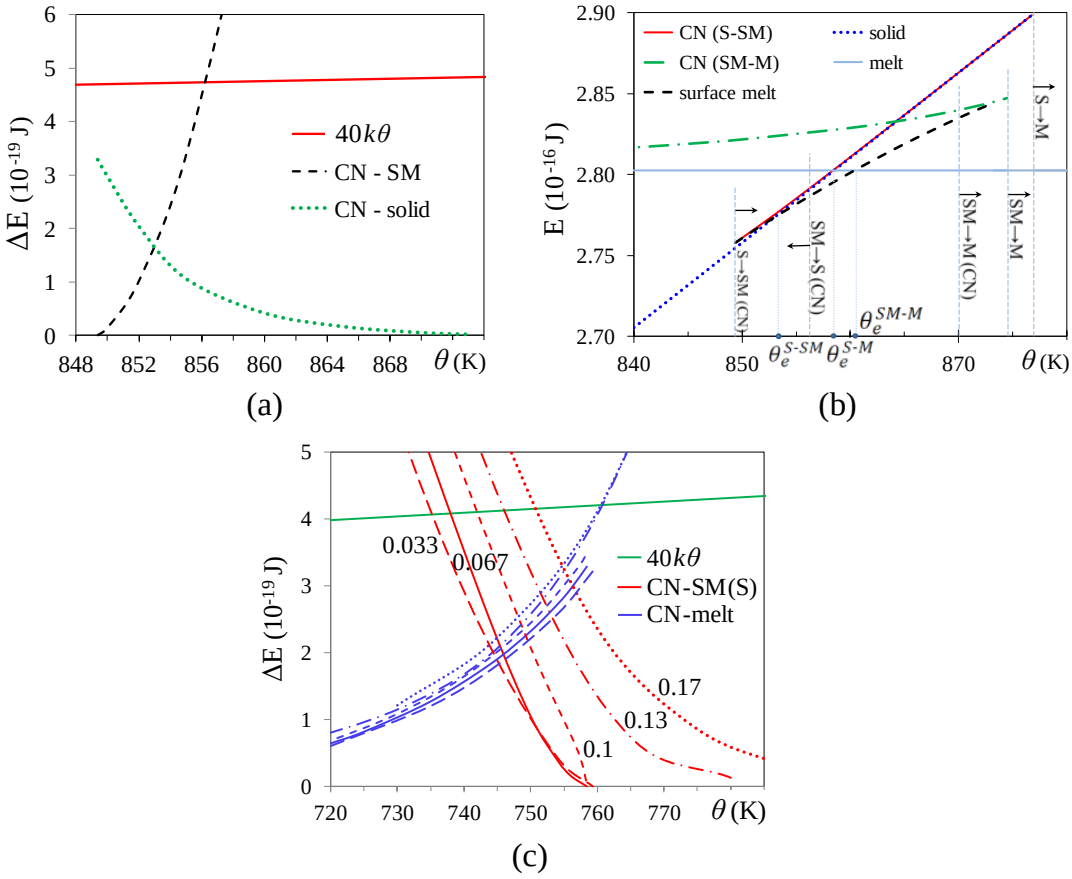

Figure 4.4 Energy difference between critical nucleus, solid and surface melt (a) and energies of solid, surface melt, melt and critical nuclei between solid and surface melt and surface melt and melt (b) for 5 nm particle with $\bar{\Delta}_\xi = 0.17$; energy difference between critical nucleus, solid (molten layer) and melt for 2 nm particle (c).

Energies of solid, surface melt, melt and critical nuclei between solid and surface

melt and surface melt and melt are shown in Fig. 4.4b. It exhibits all phase equilibrium temperatures and all transformations in different temperature ranges. As mentioned, at 849.38 K, critical nucleus and surface melt have equal energies while at 876 K which is slightly below melting temperature (877.05 K), energies of solid and critical nucleus are equal. With R = 5 nm and $\bar{\Delta}_\xi = 0.17$. Solid transforms to melt directly without appearance of surface molten layer at 877.05 K.

Next we investigated the possibility of bi-stable states between solid and melt. While for 5 nm particle with $\bar{\Delta}_\xi = 0.17$, they cannot be found, for 2 nm particle bi-stability can happen in the range $\bar{\Delta}_\xi = 0.033$ - 0.17 (Fig. 4.4c). E.g., for $\bar{\Delta}_\xi = 0.067$, temperature range for bi-stability is 738.00 K to 758.45 K; above 758.45 K, energies of critical nucleus and molten layer are equal and no CN exists, since solid transforms barrierlessly to melt. This is why for $\bar{\Delta}_\xi = 0.033$, 0.067 and 0.1, blue curves in Fig. 4.4c do not intersect with $40k\theta$ energy line. Our result for size range of bi-stability between solid and melt are in agreement with MD simulations[9], where they observed bi-stability for nanoparticles with fewer than 850 atoms (25 $\mathring{A} \approxeq$ 800 atoms). However, the bi-stability temperature range for 2 nm particle in [11], $\sim$ 525 K to 590 K is more than 200 K below our bi-stability temperature range. However, the melting temperature of $\sim$ 550 K for 2 nm particle in[9] is also 240 K below that from experiments[6]. For the 2 nm particle with $\bar{\Delta}_\xi = 0.12$, our model perfectly describes experiments (Fig. 4.2b).

Transformation diagram

Excluding barrierless two-way continuous transformations S$\leftrightarrow$SM for $\bar{\Delta}_\xi < 0.083$, all other transformations may occur via critical nuclei at smaller driving forces (Fig. 4.5). Thus all dashed lines in Fig.4.5 corresponds to the fulfillment of the criterion ΔE=40kθ for corresponding CN. In particular, along the dashed orange straight line M$\rightarrow$SM(CN) with the slope -3.488 K, homogeneous molten particle fluctuationally transforms to the SM during cooling. Similar, along the dashed blue straight line M$\rightarrow$S(CN) with the

slope -0.778 K, homogeneous molten particle fluctuationally transforms to the solid. Solidification via critical nucleus occurs 72 K above the barrierless solidification. Similar, straight dashed red lines SM→M(CN) of slope -13.46 K below $\bar{\Delta}_\xi = 0.16$ and -20.73 K for $\bar{\Delta}_\xi > 0.16$ for kinetic transformation of a surface melt to melt is approximately parallel to the similar line SM→M for barrierless melting of the surface melt and is 5.4 K below.

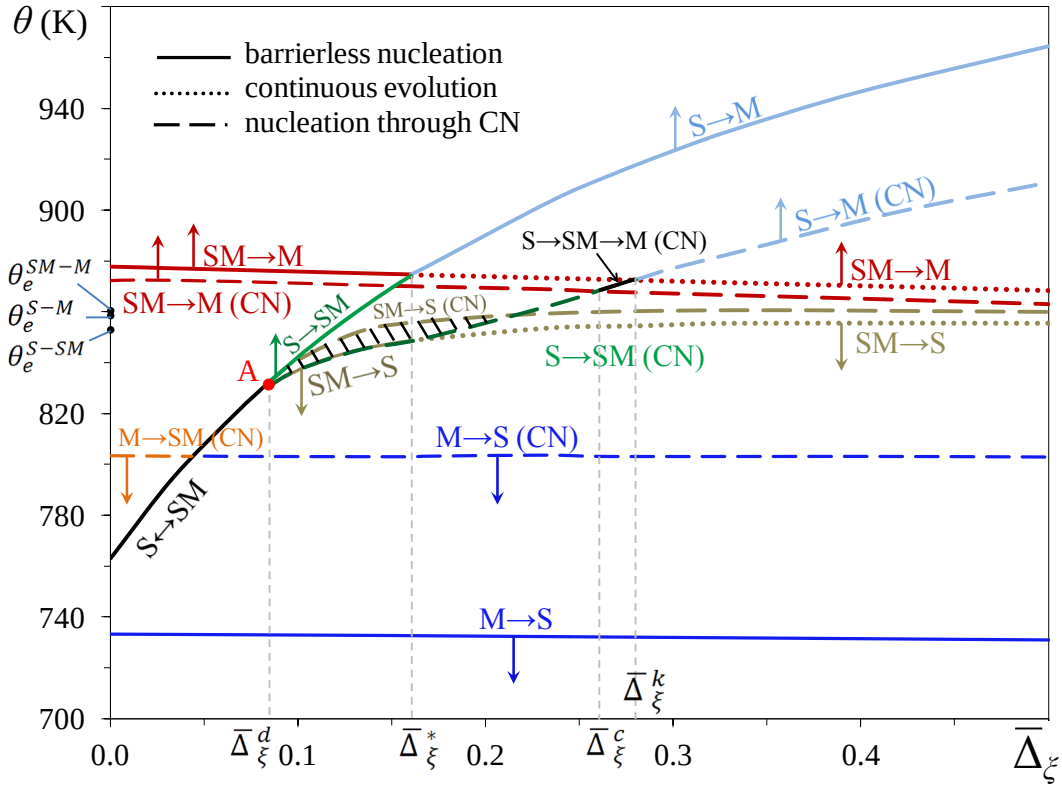

Figure 4.5 Barrierless and thermally activated transformation temperatures vs normalized surface layer thickness, $R = 5$ nm.

The line SM→S(CN) for kinetic solidification of a surface melt is 0.85 - 7.5 K above the corresponding line SM→S for barrierless solidification. As a result, temperature range for the existence of a surface melt when thermal fluctuations are taken into account is essentially narrower than for thermodynamic treatment. The line S→SM(CN), along which solid is transformed to a surface melt via critical nucleus starts from the same point A from which thermodynamic S→SM and SM→S curves and kinetic SM→S(CN)

curve exit. Close to the point A, kinetic S→SM(CN) curve practically coincides with thermodynamic curve SM→S for the opposite transformation. At point A, energy of molten layer, solid, and CN between them are equal and CN and molten layer do not exist at a lower temperature. Kinetic S→SM(CN) and barrierless SM→S curves coincide for $\bar{\Delta}_\xi^d < \bar{\Delta}_\xi < \bar{\Delta}_\xi^*$. For larger $\bar{\Delta}_\xi$, kinetic S→SM(CN) curve is essentially higher than the thermodynamic SM→S one. After the kinetic curve S→SM(CN) intersects and is above the kinetic line SM→M(CN), a double transformation occurs: first, solid transforms to a surface melt, then surface melt transforms to melt, both through critical nuclei (shown as S→SM→M). Above the doted thermodynamic line SM→M, surface melt does not exist because it melts barrierlessly. That is why along the kinetic blue line S→M(CN), solid directly melts via a critical nucleus. Remarkably, in the dashed hatched region between lines S→SM(CN) and SM→S(CN), both appearance of a surface melt at the solid surface and its reverse transition to the solid are kinetically possible. That means that system is in a bi-stable state and surface melt will spontaneously appear and disappear in time.

Interpretation of experimental melting and solidification temperatures

There are two main definitions of the melting temperature for nanoparticles in the sharp-interface approach: based on equality of the free energy of completely molten and solid or energy of melt and energy of solid with surface melt. However, due to hysteresis, these are not actual transition temperature. When barrierless surface melting was suppresses by not fulfillment of the necessary condition $\gamma_s - \gamma_l > \gamma_{sl}$, simplified kinetic approaches have been applied, e.g.,[10, 11]. They have never been applied when barrierless surface melting was possible. In the PFA[12] melting temperature also was defined by equality of the free energy of completely molten and solid. In[7, 8] we defined melting temperature as the transformation temperature at which surface melt losses its stability and transforms to complete melt. Here, in Fig. 4.1, we expended the same definition for barrierless transformations between solid, melt, and surface melt as function of $\bar{\Delta}_\xi$. Since

in Fig.4.1 thermal fluctuations are neglected, this transformation diagram is valid for very fast heating/cooling only. Fig.4.5 offers much more realistic transformation diagram for traditional heating/cooling rates, based on kinetic nucleation criterion. Since CN does not represent complete phases $\eta = 0$ or 1 but some intermediate states, and because of necessity to resolve external surface, surface melt, and solid-melt interfaces, similar kinetic sharp interface approach could not be applied.

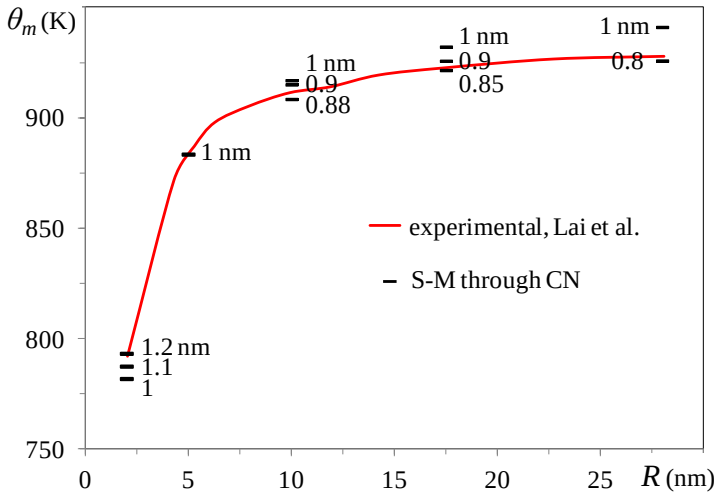

Figure 4.6 Kinetic melting temperature vs R at different $\bar{\Delta}_\xi$ values.

Kinetic results differ essentially from results based on equality of energies and barrierless nucleation. Thus, for 5 nm particles, in comparison with barrierless transformations, kinetic approach extends region when surface melt can be obtained at constant $\bar{\Delta}_\xi$ from $\bar{\Delta}_\xi^*$ to $\bar{\Delta}_\xi^k$, reduced melting temperature by 5.4 K below $\bar{\Delta}_\xi^*$ and by $5.4 - 53.7$ K above $\bar{\Delta}_\xi^*$. It also introduced kinetic transition from melt to surface melt, which cannot occur barrierlessly. Thermally activated solidification of melt occurs by 72 K higher than barrierless solidification. Comparison of predictions of the kinetic melting temperature with experiment is presented in Fig. 4.6. It allows us to choose the best value of $\bar{\Delta}_\xi^*$ for Al.

Conclusions

Melting of aluminum nanoparticles with surface layer between solid and gas is studied. The results show that neglecting the effect of surface layer can underestimate thickness of the surface molten layer and melting temperatures. Small surface layer thicknesses ($\bar{\Delta}_\xi < 0.17$) change melting temperatures only for small nanoparticles (R < 5 nm). To study the possibility of bistability between solid, surface melt and molten phases, critical nucleus between different phases was obtained. Critical nucleus increases in size with reduction of temperature. The initial non-spherical critical nucleus can change to a spherical shape at lower temperatures. While bistability is observed between solid and surface melt for 5 nm particle with $\bar{\Delta}_\xi = 0.17$, for the same model, bistability does not happen between solid and melt. Only in smaller particles (R = 2 nm) bistability appears between solid and melt, which is in agreement with MD results. The temperature range for bistability from our model is different from those obtained in MD analysis, while melting temperatures from current study are in much better agreement with experimental data than those from MD simulations.

References

1. M. A. Caldwell, R. G. D. Jeyasingh, H. S. P. Wong and D. J. Milliron, Nanoscale, 4, 4382 (2012).

2. S. Sinha-Ray , R. P. Sahu and A. L. Yarin , Soft Matter, 7, 8823-8827 (2011).

3. V. I. Levitas, Combustion and Flame, 156, 543 (2009).

4. B. F. Henson and L. Smilowitz, 844-850 (2010).

5. V. I. Levitas, Z. Ren, Y. Zeng, Z. Zhang and G. Han, Physical Review B, Rapid Communication, 85, (22), 220104(R), (2012).

6. S. L. Lai, J. R. A. Carlsson and L. H. Allen, Appl. Phys. Lett. 72, 1098 (1998).

7. V. I. Levitas V and K. Samani, Nat Commun 2, 284 (2011).

8. V. I. Levitas V and K. Samani, Physical Review B, Rapid Communication, Vol. 84, 14, 140103(R)(2011).

9. S. Alavi and D. L. Thompson, J. Phys. Chem. A, 110 (2006).

10. P. R. Couchman and W. A. Jesser, Nature, 269, 481 (1977).

11. Q. Xu, I. D. Sharp, C. W. Yuan, D. O. Yi, C. Y. Liao, A. M. Glaeser, A. M. Minor, J. W. Beeman, M. C. Ridgway, P. Kluth, J. W. Ager III, D. C. Chrzan, and E. E. Haller, Phys. Rev. Lett., 97, 155701 (2006)

12. J. Chang and E. Johnson, Philos. Mag. 85, 3617 (2005).

13. A. W. Denier van der Gon, R. J. Smith, J. M. Gay, D. OConnor and J. van der Veen, Surf. Sci. 227, 143 (1990).

14. B. F. Henson and J. M. Robinson, Phys. Rev. Lett. 92, 246107 (2004).

15. F. D. Fischer, T. Waitz, D. Vollath and N. K. Simha, Prog. Mat. Sci., 53, 481 (2008).

16. P. Puri and V. Yang, J. Phys. Chem. C, 111, 11776 (2007).

17. V. I. Levitas and M. Javanbakht, Phys Rev Lett, 107, 175701 (2011).

CHAPTER 5. GENERAL CONCLUSIONS

General Discussion

To study melting related phenomena in aluminum nanoparticles, We developed an advanced phase field model coupled to mechanics. In chapter 2, Melting temperature and thickness of surface molten layer were compared to experimental results and good agreements were observed. Indeed melting temperatures from our model are in better agreement with experiments compared to molecular dynamics results. Although the sharp interface approach can be used for melting of nanoparticles, but when the interface thickness is comparable to particle size, the phase field approach is more precise. Also for fast heating rate problems, only the phase field approach can predict the homogeneous melting of the particle. The coherent solid-melt model was proved to be valid for melting related problems, but it was also shown more advanced models are needed to compensate the terms that suppress melting. For this, in chapter 3, deviatoric transformation strain was added to the model to relax the elastic energy, which suppresses melting. Different interface stress distributions similar to those from molecular dynamics simulations were obtained.

In chapter 4, transition between particle and surrounding at the external surface was included in the model. It was shown that the melting temperature is strongly dependent on the thickness of the external surface layer thickness. Both barrierless and thermally activated melting via critical nucleus were studied and transformation diagram for different transitions between solid, surface melt and melt was obtained. These results

open new directions for controlling melting-related phenomena by controlling the surface layer thickness and its interaction with the surrounding.